

Riemann Solver for a Kinematic Wave Traffic Model with Discontinuous Flux[☆]

Jeffrey K. Wiens^{a,*}, John M. Stockie^a, JF Williams^a

^a*Department of Mathematics, Simon Fraser University, 8888 University Drive, Burnaby, BC, Canada, V5A 1S6*

Abstract

We investigate a model for traffic flow based on the Lighthill–Whitham–Richards model that consists of a hyperbolic conservation law with a discontinuous, piecewise-linear flux. A mollifier is used to smooth out the discontinuity in the flux function over a small distance $\epsilon \ll 1$ and then the analytical solution to the corresponding Riemann problem is derived in the limit as $\epsilon \rightarrow 0$. For certain initial data, the Riemann problem can give rise to *zero waves* that propagate with infinite speed but have zero strength. We propose a Godunov-type numerical scheme that avoids the otherwise severely restrictive CFL constraint that would arise from waves with infinite speed by exchanging information between local Riemann problems and thereby incorporating the effects of zero waves directly into the Riemann solver. Numerical simulations are provided to illustrate the behaviour of zero waves and their impact on the solution. The effectiveness of our approach is demonstrated through a careful convergence study and comparisons to computations using a third-order WENO scheme.

Keywords: Hyperbolic conservation law, Discontinuous flux, Traffic flow, Lighthill–Whitham–Richards model, Finite volume scheme, Zero waves
2010 MSC: 35L65, 35L67, 35R05, 65M08, 76L05

1. Introduction

In the 1950's, Lighthill and Whitham [30] and Richards [36] independently proposed the first macroscopic traffic flow model, now commonly known as the LWR model. Although this model has proven successful in capturing some aspects of traffic behaviour, its limitations are well-documented and many more sophisticated models have been proposed to capture the complex dynamics and patterns observed in actual vehicular traffic [22]. Despite this progress, the LWR model remains an important and widely-used model because of its combination of simplicity and explanatory power.

[☆]This work was supported by two Discovery Grants from the Natural Sciences and Engineering Research Council of Canada (NSERC).

*Corresponding author.

Email addresses: jwiens@sfu.ca (Jeffrey K. Wiens), jstockie@sfu.ca (John M. Stockie), jfwillia@sfu.ca (JF Williams)

URL: <http://www.math.sfu.ca/~stockie> (John M. Stockie)

Preprint submitted to Journal of Computational Physics

August 30, 2021

9 The LWR model consists of a single scalar nonlinear conservation law in one dimension

$$\rho_t + f(\rho)_x = 0, \quad (1)$$

where $\rho(x, t)$ is the traffic density (cars/m),

$$f(\rho) = \rho v(\rho)$$

10 is the traffic flow rate or flux (cars/sec), and $v(\rho)$ is the local velocity (m/sec). The most
11 commonly used flux function is

$$f(\rho) = u_{max} \rho \left(1 - \frac{\rho}{\rho_{max}} \right), \quad (2)$$

12 which was obtained by Greenshields [20] in the 1930's by fitting experimental measure-
13 ments of vehicle velocity and traffic density. Here, u_{max} is the maximum free-flow speed,
14 while ρ_{max} is the maximum density corresponding to bumper-to-bumper traffic where
15 speed drops to zero. The LWR model belongs to a more general class of *kinematic wave*
16 *traffic models* that couple the conservation law Eq. (1) with a variety of different flux
17 functions.

18 Extensive studies of the empirical correlation between flow rate and density have
19 been performed in the traffic flow literature. This correlation is commonly referred to
20 as the *fundamental diagram* and is represented graphically by a plot of flux f versus
21 density ρ such as that shown in Fig. 1. A striking feature of many experimental results
22 is the presence of an apparent discontinuity that separates the free flow (low density)
23 and congested (high density) states, something that has been discussed by many authors,
24 including [7, 14, 15, 23]. In particular, Koshi et al. [24] characterize flux data such as
25 that shown in Fig. 1 as having a *reverse lambda* shape in which the discontinuity appears
26 at some peak value of the flux.

27 This behavior is also referred to as the *two-capacity* or *dual-mode phenomenon* [3, 4]
28 and has led to the development of a diverse range of mathematical models. Zhang and
29 Kim [41] incorporated the capacity drop into a microscopic car-following model that
30 generates fundamental diagrams with the characteristic reverse-lambda shape. Wong
31 and Wong [38] performed simulations using a multi-class LWR model from which they
32 also observed a discontinuous flux-density relationship. Colombo [8] and Goatin [17]
33 developed a macroscopic model that couples an LWR equation for density in the free
34 flow state, along with a 2×2 system of conservation laws for density and momentum in
35 the congested state; the phase transition between these two states is a free boundary
36 that is governed by the Rankine-Hugoniot conditions. Lu et al. [31] incorporated a
37 discontinuous (piecewise quadratic) flux directly into an LWR model, and then solved
38 the corresponding Riemann problem analytically by constructing the convex hull for a
39 regularized continuous flux function that consists of two quadratic pieces joined over a
40 narrow region by a linear connecting piece.

41 There remains some disagreement in the literature regarding the existence of dis-
42 continuities in the traffic flux, with some researchers (e.g., Hall [21]) arguing that the
43 apparent gaps are due simply to missing data and can be accounted for by providing
44 additional information about traffic behaviour at specific locations. Indeed, Persaud and
45 Hall [35] and Wu [39] contend that the discontinuous fundamental diagram should be
46 viewed instead as the 2D projection of a higher dimensional smooth surface.

47 We will nonetheless make the assumption in this paper that the fundamental diagram
 48 is discontinuous. Our aim here is not to argue the validity of this assumption in the
 49 context of traffic flow, since that point has already been discussed extensively by [31,
 50 38, 41], among others. Instead our objective is to study the effect that such a flux
 51 discontinuity has on the analytical solution of a 1D hyperbolic conservation law, as well
 52 as to develop an accurate and efficient numerical algorithm to simulate such problems.

53 A related class of conservation laws, in which the flux $f(\rho, x)$ is a discontinuous func-
 54 tion of the spatial variable x , has been thoroughly studied in recent years (see [5, 6] and
 55 the references therein). Considerably less attention has been paid to the situation where
 56 the flux function has a discontinuity in ρ . Gimse [16] solved the Riemann problem for a
 57 piecewise linear flux function with a single jump discontinuity in ρ by generalizing the
 58 method of convex hull construction [28, Ch. 16]. In particular, Gimse identified the exis-
 59 tence of *zero shocks*, which are discontinuities in the solution that carry no information
 60 and have infinite speed of propagation. We note that more recently, Armbruster et al. [1]
 61 observed *zero rarefaction waves* with infinite speed of propagation in their study of supply
 62 chains with finite buffers (although they did not refer to them using this terminology).

63 Gimse's results were improved on by Dias and Figueira [11], who used a mollifier
 64 function η_ϵ to smooth out discontinuities in the flux function over an interval of width
 65 $0 < \epsilon \ll 1$ before constructing the convex hull using standard techniques. Solutions to
 66 the mollified problem were proven to converge to solutions of the original problem in the
 67 limit as $\epsilon \rightarrow 0$ [11]. Dias and Figueira's framework has also been applied to problems
 68 involving fluid phase transitions [10, 13] and viscoelasticity [12].

69 In this paper, we apply Dias and Figueira's mollification approach to solving a conser-
 70 vation law with a piecewise linear flux function $f(\rho)$ in which there is a single discontinuity
 71 at $\rho = \rho_m$ (see Fig. 1). The model equations and their relevance in the context of traffic
 72 flow are discussed in Section 2. We introduce a mollified flux function $f_\epsilon(\rho)$ in Section
 73 3 and verify its convexity, which then permits us to derive the analytical solution to the
 74 Riemann problem using the method of convex hull construction.

75 In Section 4, we consider the special case where either of the two constant initial
 76 states in the Riemann problem equals ρ_m , the density at the discontinuity point. This
 77 is precisely the case when a rarefaction wave of strength $O(\epsilon)$ and speed $O(1/\epsilon)$ arises,
 78 which approaches a zero rarefaction in the limit of vanishing ϵ . There are two issues that
 79 need to be addressed regarding these zero waves. First, we consider the convergence of the
 80 mollified solution to that of the original problem, since Dias and Figueira's convergence
 81 results [11] do not consider (nor easily extend to) the case when the left or right initial
 82 states in the Riemann problem are identical to ρ_m . Secondly, we discuss the physical
 83 relevance of an infinite speed of propagation in the context of traffic flow.

84 The remainder of the paper is focused on constructing a Riemann solver that forms
 85 the basis for a high resolution finite volume scheme of Godunov type. Because zero waves
 86 travel at infinite speed, the usual CFL restriction suggests that choosing a stable time step
 87 might not be possible. Some authors have avoided this difficulty by using an implicit time
 88 discretization [33], but this approach introduces added expense and complication in the
 89 numerical algorithm. Another approach employed in [1] is to replace the discontinuous
 90 flux by a regularized (continuous) function which joins the discontinuous pieces by a linear
 91 connection over an interval of width $\epsilon \ll 1$, after which standard numerical schemes may
 92 be applied; however, this approach requires a small ϵ to achieve reasonable accuracy
 93 resulting in a severe time step restriction.

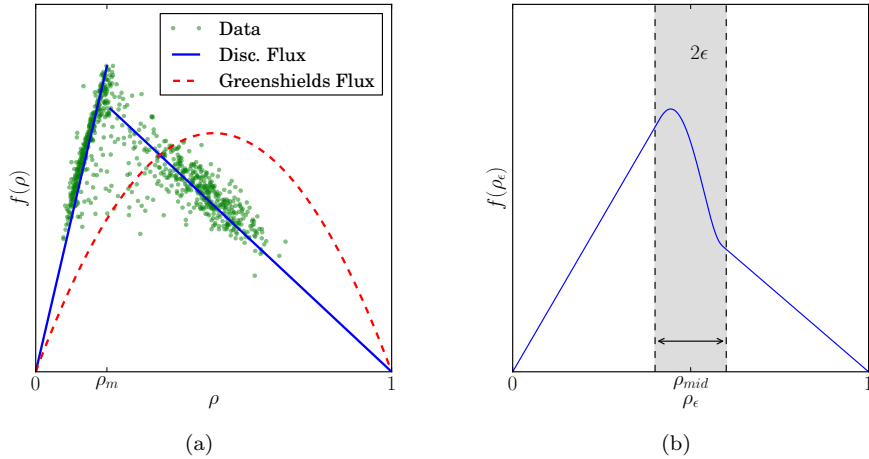


Figure 1: In (a), the discontinuous “reverse lambda” flux function Eq. (4) is overlaid with empirical data extracted from [21, Fig. 7] (reproduced with permission of Elsevier B.V.), along with the quadratic Greenshields flux (2). The mollified flux from Eq. (7) is depicted in (b).

94 We use an alternate approach that eliminates the severe CFL constraint by incorpo-
 95 rating the effect of zero waves directly into the local Riemann solver. In the process, we
 96 find it necessary to construct solutions to a subsidiary problem that we refer to as the
 97 *double Riemann problem*, which introduces an additional intermediate state correspond-
 98 ing to the discontinuity value $\rho = \rho_m$. A similar approach was used by Gimse [16] who
 99 constructed a first-order variant of Godunov’s method, although he omitted to perform
 100 any computations using his proposed method. We improve upon Gimse’s work in three
 101 ways: first, we solve the double Riemann problem within Dias and Figueira’s mollifica-
 102 tion framework; second, we implement a high resolution variant of Godunov’s scheme to
 103 increase the spatial accuracy; and third, we provide extensive numerical computations
 104 and a careful convergence study to demonstrate the effectiveness of our approach.

105 2. Mathematical Model

106 We are concerned in this paper with the scalar conservation law

$$\rho_t + f(\rho)_x = 0, \quad (3)$$

107 having a discontinuous flux function

$$f(\rho) = \begin{cases} g_f(\rho), & \text{if } 0 \leq \rho < \rho_m, \\ g_c(\rho), & \text{if } \rho_m \leq \rho \leq 1, \end{cases} \quad (4)$$

that is depicted in Fig. 1(a). The vehicle density $\rho(x, t)$ is normalized so that $0 \leq \rho \leq 1$, and ρ_m is the point of discontinuity in the flux $f(\rho)$. We restrict the flux to be a piecewise

linear function in which the free flow branch has

$$g_f(\rho) = \rho,$$

and the congested flow branch has

$$g_c(\rho) = \gamma(1 - \rho).$$

108 Experimental data suggests that $g_f(\rho_m) > g_c(\rho_m)$, and so we impose the constraint

$$0 < \gamma < \frac{\rho_m}{1 - \rho_m}. \quad (5)$$

109 We utilize the mollifier approach of Dias and Figueira [11] in order to approximate
110 the original equation (3) by

$$\frac{\partial \rho_\epsilon}{\partial t} + \frac{\partial f_\epsilon(\rho_\epsilon)}{\partial x} = 0, \quad (6)$$

111 where the mollified flux (pictured in Fig. 1(b)) is

$$f_\epsilon(\rho_\epsilon) = \rho_\epsilon + (\gamma - (\gamma + 1)\rho_\epsilon) \int_{\rho_m - \epsilon}^{\rho_\epsilon} \eta_\epsilon(s - \rho_m) ds, \quad (7)$$

112 with $0 < \epsilon \ll 1$. The mollifier function is given by $\eta_\epsilon(s) = \frac{1}{\epsilon}\eta(s/\epsilon)$, where $\eta(s)$ is a
113 *canonical mollifier* that satisfies the following conditions:

- 114 (i) $\eta \geq 0$;
- 115 (ii) $\eta \in C^\infty(\mathbb{R})$ and is compactly supported on $[-1, 1]$;
- 116 (iii) $\eta(-s) = \eta(s)$ for all $s \in \mathbb{R}$; and
- 117 (iv) $\int_{-\infty}^{\infty} \eta(s) ds = 1$.

118 The results in Dias and Figueira [11] guarantee that any mollifier satisfying the above
119 criteria converges to the same unique solution in the limit $\epsilon \rightarrow 0$. We use the following
120 mollifier

$$\eta(s) = \begin{cases} C \exp\left(\frac{1}{s^2-1}\right), & \text{if } |s| < 1, \\ 0, & \text{if } |s| \geq 1, \end{cases} \quad (8)$$

121 where $C \approx 2.2522836\dots$ is a constant determined numerically so that condition (iv)
122 holds; this choice is made for reasons of analytical convenience since the derivative η' can
123 be written in terms of η .

124 Because the mollified flux function is smooth, the conservation law (6) may now
125 be solved using standard techniques. We note that in the context of traffic flow, a
126 potential problem arises when applying the usual Oleřnik entropy condition [34] as the
127 selection principle to enforce uniqueness. Although Oleřnik's entropy condition does
128 yield the physically-correct weak solution in the context of fluid flow applications, it
129 does not always do so for kinematic wave models of traffic flow (see LeVeque [27], for
130 example). In particular, applying Oleřnik's entropy condition can lead to a solution that
131 is not anisotropic [9], corresponding to the non-physical situation where drivers react to
132 vehicles both in front *and behind*.

Zhang [40] suggests two additional criteria on the flux function to guarantee anisotropic flows in kinematic wave traffic models. First, the characteristic velocity should be smaller than the vehicle speed $v(\rho) = f(\rho)/\rho$. That is, we require

$$\frac{f(\rho)}{\rho} \geq f'(\rho), \quad \forall 0 \leq \rho \leq 1.$$

Secondly, all elementary waves must travel more slowly than the vehicles carrying them, or

$$\min\left(\frac{f(\rho_l)}{\rho_l}, \frac{f(\rho_r)}{\rho_r}\right) \geq \frac{f(\rho_r) - f(\rho_l)}{\rho_r - \rho_l},$$

for all $0 \leq \rho_l, \rho_r \leq 1$. As shown in [37], our flux function (4) satisfies both of these conditions and therefore it is reasonable to apply the Oleinik entropy condition as the selection criterion for our traffic flow model.

3. Exact Solution of the Riemann Problem with Mollified Flux

We next construct and analyze the solution $\rho_\epsilon(x, t)$ of the mollified Riemann problem, which consists of the conservation law (6) along with flux (7) and piecewise constant initial conditions

$$\rho_\epsilon(x, 0) = \begin{cases} \rho_l, & \text{if } x < 0, \\ \rho_r, & \text{if } x \geq 0. \end{cases}$$

This problem can be solved using the method of convex hull construction [28, Ch. 16] which requires knowledge of the inflection points of the mollified flux $f_\epsilon(\rho_\epsilon)$. Using Eq. (8), the first and second derivatives of the flux are

$$f'_\epsilon(\rho_\epsilon) = 1 + [\gamma - (\gamma + 1)\rho_\epsilon] \eta_\epsilon(\rho_\epsilon - \rho_m) - (\gamma + 1) \int_{\rho_m - \epsilon}^{\rho_\epsilon} \eta_\epsilon(s - \rho_m) ds, \quad (9)$$

$$f''_\epsilon(\rho_\epsilon) = \kappa(\rho_\epsilon) \left[\left(\frac{\gamma}{\gamma + 1} - \rho_\epsilon \right) (\rho_m - \rho_\epsilon) - \epsilon^2 \left[\left(\frac{\rho_\epsilon - \rho_m}{\epsilon} \right)^2 - 1 \right]^2 \right], \quad (10)$$

where

$$\kappa(\rho_\epsilon) = \frac{2\eta_\epsilon(\rho_\epsilon - \rho_m)}{\epsilon^2(\gamma + 1) \left[\left(\frac{\rho_\epsilon - \rho_m}{\epsilon} \right)^2 - 1 \right]^2}.$$

Since the mollifier has compact support, we know that there can be no inflection points outside the smoothing region of width 2ϵ ; that is, $f''_\epsilon(\rho_\epsilon) \equiv 0$ when $|\rho_\epsilon - \rho_m| \geq \epsilon$. Also, since $\kappa(\rho_\epsilon) > 0$, the convexity of f_ϵ is determined solely by the sign of the quantity

$$P(\rho_\epsilon) = \left(\frac{\gamma}{\gamma + 1} - \rho_\epsilon \right) (\rho_m - \rho_\epsilon) - \epsilon^2 \left[\left(\frac{\rho_\epsilon - \rho_m}{\epsilon} \right)^2 - 1 \right]^2, \quad (11)$$

which we analyze next.

Since Eq. (11) is a quartic polynomial in ρ_ϵ , analytic expressions are available for the roots; however, these are too complicated for our purposes. Instead, we take advantage of the scaling properties of the polynomial to simplify P and rewrite Eq. (11) as

$$P(y) = -\frac{1}{\epsilon^2} y^4 + 3y^2 + My - \epsilon^2, \quad (12)$$

144 where $y = \rho_\epsilon - \rho_m \in [-\epsilon, \epsilon]$ and $M = \rho_m - \gamma/(\gamma + 1)$. Clearly $|y| = |\rho_\epsilon - \rho_m| < \epsilon$, and
 145 so it is natural to suppose that $y = O(\epsilon^\lambda)$ with $\lambda \geq 1$, after which the various terms in
 146 Eq. (12) have the scalings indicated below:

$$P(y) = \underbrace{-\frac{1}{\epsilon^2}y^4}_{O(\epsilon^{4\lambda-2})} + \underbrace{3y^2}_{O(\epsilon^{2\lambda})} + \underbrace{My}_{O(\epsilon^\lambda)} - \underbrace{\epsilon^2}_{O(\epsilon^2)}. \quad (13)$$

Since M is a constant that is independent of ϵ , we can take $M = O(1)$ as $\epsilon \rightarrow 0$. Guided by the scalings in Eq. (13), the dominant terms in $P(y)$ are the last two terms having orders $O(\epsilon^\lambda)$ and $O(\epsilon^2)$. When ϵ is sufficiently small, we may therefore neglect the remaining terms and determine the convexity of f_ϵ based on the sign of the simpler linear polynomial

$$P_1(y) = My - \epsilon^2,$$

which has a single root at $y = \epsilon^2/M$ corresponding to $\rho_\epsilon = \rho_m + \epsilon^2/M$. For values of y close enough to ϵ^2/M , higher order terms in the polynomial $P(y)$ become significant and could potentially introduce additional roots; however, by continuing this method of dominant balance, we find that $P(y)$ maintains the single root at higher orders as well, which we demonstrate numerically using the plots of P summarized in Fig. 2. Based on this argument and the observation that inequality (5) requires $M > 0$, we can conclude that

$$f''_\epsilon(\rho_\epsilon) \geq 0 \quad \text{when} \quad \rho_\epsilon \in [\rho_m, 1],$$

and

$$f''_\epsilon(\rho_\epsilon) \leq 0 \quad \text{when} \quad \rho_\epsilon \in [0, \rho_m].$$

147 Therefore, the mollified flux function has a single inflection point at $\rho_\epsilon = \rho_m + O(\epsilon^2)$ as
 148 $\epsilon \rightarrow 0$, where the slope $f'_\epsilon(\rho_m) \rightarrow -\infty$. Since the flux derivative $f'(\rho)$ corresponds to the
 149 elementary wave speed in the Riemann problem, this same point ρ_m is also the source of
 150 the infinite speed of propagation which will be analyzed in more detail in Section 4.

151 Using this information, we can now construct the convex hull of the flux function
 152 $f_\epsilon(\rho_\epsilon)$ which is then used to solve the Riemann problem. There are three non-trivial
 153 cases to consider, depending on the left and right initial states, ρ_l and ρ_r . Two of these
 154 cases (which we call A and B) lead to the emergence of a new constant intermediate
 155 state with density ρ_m . This ‘‘plateau’’ is a characteristic feature of solutions to our LWR
 156 model with discontinuous flux.

157

158 **Case A:** $\rho_r < \rho_m < \rho_l$.

Here we construct the smallest convex hull of the set $\{(\rho_\epsilon, y) : \rho_r < \rho_\epsilon < \rho_l \text{ and } y \leq f_\epsilon(\rho_\epsilon)\}$, which as shown in Fig. 3(a) must consist of three pieces. The first piece corresponds to a contact line that follows $f_\epsilon(\rho_\epsilon)$ on the left up to the point $\rho_* \in (\rho_m - \epsilon, \rho_m)$ for which the shock and characteristic speeds are equal; that is,

$$s = \frac{f_\epsilon(\rho_l) - f_\epsilon(\rho_*)}{\rho_l - \rho_*} = f'_\epsilon(\rho_*).$$

159 The third piece of the convex hull corresponds to a shock that connects the states ρ_* and
 160 ρ_l . The middle piece, in between the contact line and shock, gives rise to a rarefaction
 161 wave that follows the curved portion of the flux in the neighbourhood of ρ_m . Based on

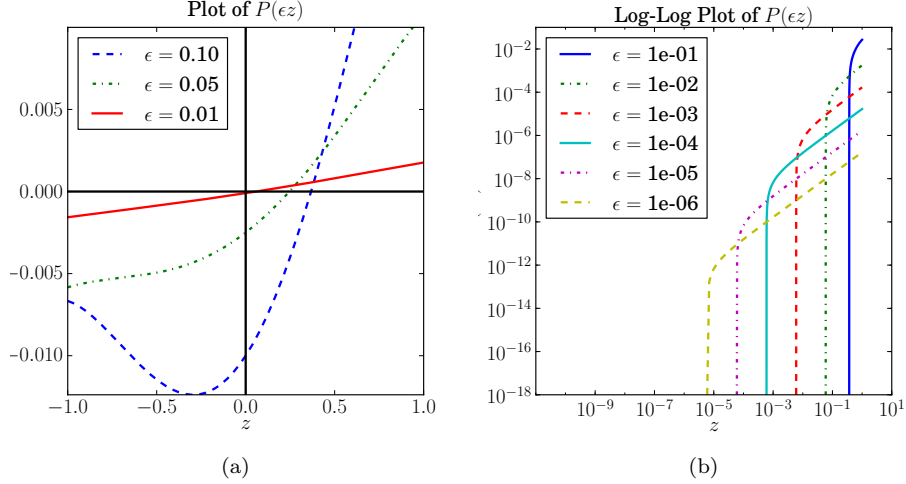


Figure 2: Plots of the function $P(\epsilon z)$ and its roots for different ϵ when $\gamma = 0.5$ and $\rho_m = 0.5$.

162 this convex hull, we can then construct the solution profile shown in Fig. 3(b). Since the
 163 rarefaction wave consists of density values bounded between $\rho_m - \epsilon$ and $\rho_m + \epsilon$, this wave
 164 flattens out and degenerates to a constant intermediate state ρ_m in the limit as $\epsilon \rightarrow 0$.

165 To summarize, in the limit as $\epsilon \rightarrow 0$ the solution to the Riemann problem when
 166 $\rho_r < \rho_m < \rho_l$ is

$$\rho(x, t) = \begin{cases} \rho_l, & \text{if } x < st, \\ \rho_m, & \text{if } st \leq x \leq t, \\ \rho_r, & \text{if } x > t, \end{cases} \quad (14)$$

167 consisting of a 1-shock moving to the left with speed

$$s = \frac{f(\rho_l) - g_f(\rho_m)}{\rho_l - \rho_m} < 0, \quad (15)$$

168 and a 2-contact moving to the right with speed 1.

169

170 **Case B:** $\gamma/(\gamma + 1) < \rho_l < \rho_m < \rho_r$.

In contrast with the previous case, we now have $\rho_l < \rho_r$ and so the convex hull $\{(\rho_\epsilon, y) : \rho_l < \rho_\epsilon < \rho_r \text{ and } y \geq f_\epsilon(\rho_\epsilon)\}$ lies above the flux-density curve as shown in Fig. 4(a). The first piece of the convex hull corresponds to a shock wave connecting the states ρ_l and $\rho_* \in (\rho_m - \epsilon, \rho_m)$, while the third piece follows the portion of the flux function in the region $[\rho_*, \rho_r]$. As before, the state ρ_* is chosen so that the shock and characteristic speeds are equal:

$$s = \frac{f_\epsilon(\rho_*) - f_\epsilon(\rho_l)}{\rho_* - \rho_l} = f'_\epsilon(\rho_*).$$

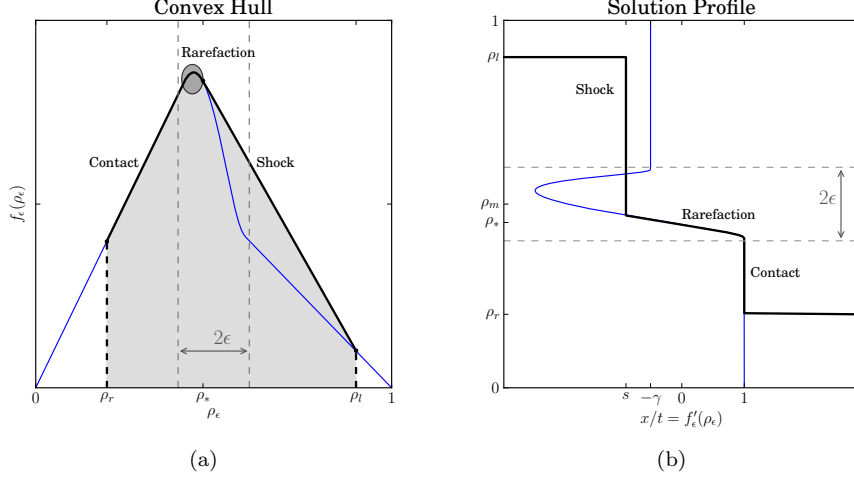


Figure 3: The convex hull construction for Case A. (a) The thin (blue) line is the mollified flux function $f_\epsilon(\rho_\epsilon)$ and the thick (black) line is the convex hull. The shaded oval region highlights the rarefaction wave. (b) The solution $\rho_\epsilon(x/t)$ is shown as a thick (black) line, along with the corresponding flux derivative $f'(\rho)$ as a thin (blue) line. Parameter values are $\rho_l = 0.9$, $\rho_r = 0.2$, $\rho_m = 0.5$, $\epsilon = 0.1$ and $\gamma = 0.5$.

171 The resulting solution profile in the limit as $\epsilon \rightarrow 0$ is pictured in Fig. 4(b):

$$\rho(x, t) = \begin{cases} \rho_l, & \text{if } x < st, \\ \rho_m, & \text{if } st \leq x \leq -\gamma t, \\ \rho_r, & \text{if } x > -\gamma t, \end{cases} \quad (16)$$

172 which consists of a 1-shock moving to the left with speed

$$s = \frac{g_c(\rho_m) - f(\rho_l)}{\rho_m - \rho_l} < 0, \quad (17)$$

173 and a 2-contact moving to the left with speed $-\gamma$.

174

175 **Case C: $\rho_l < \rho_m < \rho_r$ and $\gamma/(\gamma + 1) \geq \rho_l$.**

176 The solution structure in this case is significantly simpler than the previous two in that
 177 there is only a single shock connecting the states ρ_r and ρ_l , and hence no intermediate
 178 state. The convex hull is depicted in Fig. 5(a) and the corresponding solution profile in
 179 Fig. 5(b). As $\epsilon \rightarrow 0$, the solution reduces to

$$\rho_\epsilon(x, t) = \begin{cases} \rho_l, & \text{if } x < st, \\ \rho_r, & \text{if } x \geq st, \end{cases} \quad (18)$$

180 which corresponds to a shock with speed

$$s = \frac{f(\rho_r) - f(\rho_l)}{\rho_r - \rho_l}, \quad (19)$$

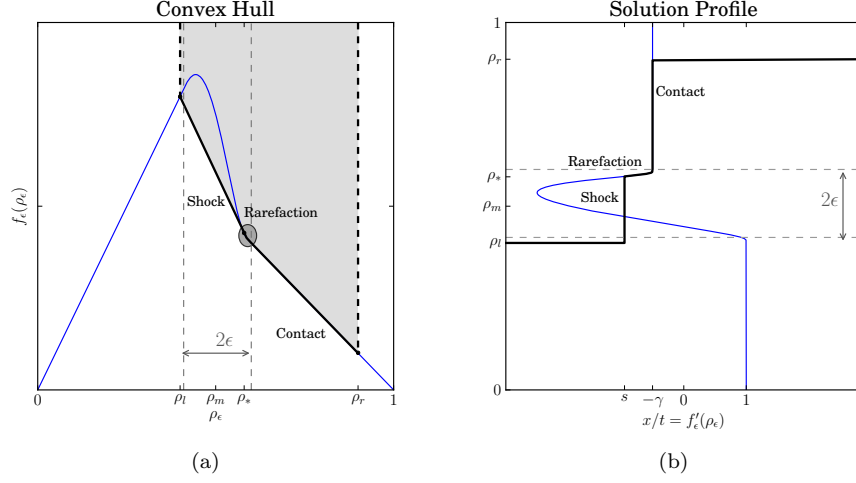


Figure 4: The convex hull construction for Case B. (a) The thin (blue) line is the mollified flux function $f_\epsilon(\rho_\epsilon)$ and the thick (black) line is the convex hull. The shaded oval region highlights the rarefaction wave. (b) The solution $\rho_\epsilon(x/t)$ is shown as a thick (black) line, along with the corresponding flux derivative $f'(\rho)$ as a thin (blue) line. Parameter values are $\rho_l = 0.4$, $\rho_r = 0.9$, $\epsilon = 0.1$, $\gamma = 0.5$, $\rho_m = 0.5$.

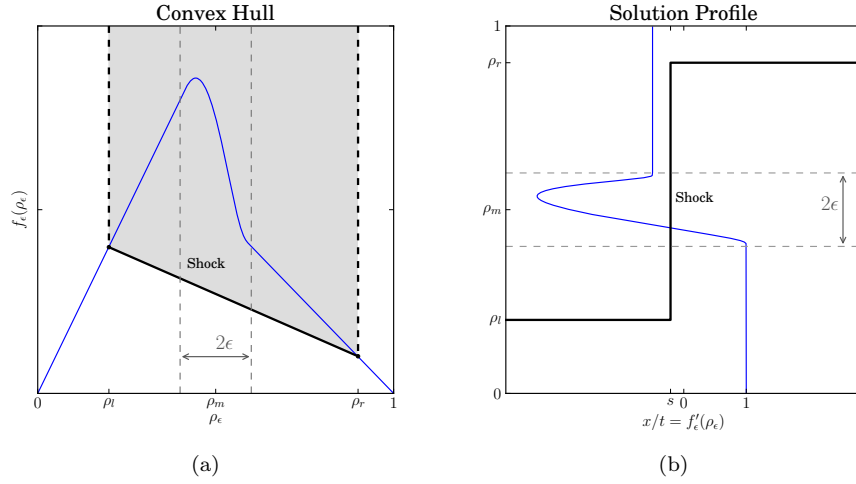


Figure 5: The convex hull construction for Case C. (a) The thin (blue) line is the mollified flux function $f_\epsilon(\rho_\epsilon)$ and the thick (black) line is the convex hull. The shaded oval region highlights the rarefaction wave. (b) The solution $\rho_\epsilon(x/t)$ is shown as a thick (black) line, along with the corresponding flux derivative $f'(\rho)$ as a thin (blue) line. Parameter values are $\rho_l = 0.2$, $\rho_r = 0.9$, $\rho_m = 0.5$, $\epsilon = 0.1$ and $\gamma = 0.5$.

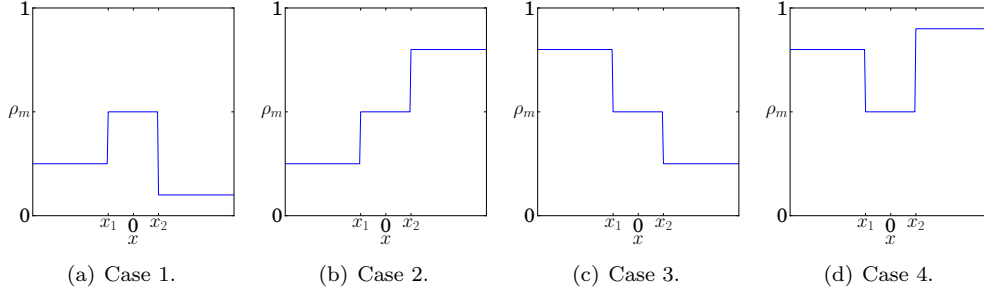


Figure 6: Four possible cases for the initial conditions of the double Riemann problem (20).

181 which can be either positive or negative depending on the sign of the numerator.

182 Note that as ρ_l or ρ_r approaches the discontinuity ρ_m , the Riemann solution becomes
 183 sensitive to the choice of initial data. This sensitivity is not unique to our problem, but is
 184 also observed in other analytical solutions for problems with discontinuous flux, such as
 185 in [13, 16, 31]. In the context of traffic flow, this sensitivity occurs in the neighbourhood
 186 of the transition point between free-flow and congested traffic, the exact location of which
 187 is expected to be highly sensitive to the state of individual drivers comprising the flow.
 188 Therefore, the sensitivity in our model is consistent with actual traffic.

189 4. Analysis of Zero Waves

190 In this section, we consider the two special situations that were not addressed in
 191 Section 3, namely where either $\rho_l = \rho_m$ or $\rho_r = \rho_m$. In both cases, the mollified problem
 192 gives rise to a wave having speed $O(1/\epsilon)$ and strength $O(\epsilon)$, which we refer to as a *zero*
 193 *rarefaction wave* because of its similarity to the zero shocks identified by Gimse [16].
 194 Since the speed of these waves becomes infinite as $\epsilon \rightarrow 0$, information can be exchanged
 195 instantaneously between neighbouring Riemann problems in any Godunov-type method.
 196 We demonstrate in this section how these effects can be incorporated into the local
 197 Riemann solver.

198 Motivated by the need to consider interactions between Riemann problems arising
 199 from two pairs of piecewise constant states, we consider a *double Riemann problem* consist-
 200 ing of two “usual” Riemann problems: one on the left with $(\rho_l, \rho_r) = (C_l, \rho_m)$, and a
 201 second on the right with $(\rho_l, \rho_r) = (\rho_m, C_r)$. As a result, the mollified conservation law
 202 (6) is supplemented with the following piecewise constant initial data pictured in Fig. 6

$$\rho_\epsilon(x, 0) = \begin{cases} C_l, & \text{if } x < x_1, \\ \rho_m, & \text{if } x_1 \leq x \leq x_2, \\ C_r, & \text{if } x > x_2, \end{cases} \quad (20)$$

203 where we have used the notation C_l and C_r for the left/right states to emphasize the
 204 fact that we are solving a double Riemann problem.

205 Since the solution can contain waves whose speed becomes unbounded, it follows
 206 that we cannot solve the double Riemann problem with intermediate state ρ_m by simply

207 splitting the solution into two local Riemann problems and applying standard techniques.
 208 Instead, the origin and dynamics of zero waves need to be considered when constructing
 209 the solution. The double Riemann problem with a mollified flux consists of up to three
 210 separate waves. Two of the waves – which we call the 1- and 2- wave using the standard
 211 terminology – correspond respectively to the left-most (x_1) and right-most (x_2) waves
 212 arising from the initial discontinuities in the double Riemann problem. We will see later
 213 that the 1-wave is a shock and the 2-wave is a contact line. The third wave corresponds
 214 to a left-moving rarefaction wave having strength $O(\epsilon)$ and speed $O(1/\epsilon)$ that originates
 215 from the x_2 interface and is located between the other two waves. As $\epsilon \rightarrow 0$, the
 216 rarefaction wave approaches a zero wave that mediates an *instantaneous* interaction
 217 between the 1- and 2-waves.

218 4.1. Origin of Zero Waves

219 Since the local Riemann problem arising at the 2-wave (i.e., the contact line at the x_2
 220 interface) is the source of the zero rarefaction wave, we begin by focusing our attention
 221 on the right half of the double Riemann problem. The formation of a zero wave at the
 222 discontinuity in the initial data located at x_2 can be divided into two cases, corresponding
 223 to whether $C_r < \rho_m$ or $C_r > \rho_m$. The specifics of the interaction between the 1-shock
 224 and the zero wave will be treated separately Section 4.2.

225 **Zero rarefaction with $C_r < \rho_m$ and $C_l = \rho_m$.**

226 We first consider the mollified Riemann problem with $C_l = \rho_l = \rho_m$ and $C_r = \rho_r <$
 227 ρ_m . The convex hull and solution profile shown in Fig. 7 exhibit a right-moving contact
 228 line (the 2-wave) having speed $s = 1$ and a rarefaction wave of strength $O(\epsilon)$ travelling to
 229 the left with speed $O(1/\epsilon)$. For a simple isolated Riemann problem, the solution would
 230 reduce to a lone contact line as $\epsilon \rightarrow 0$ and the zero rarefaction would have no impact.
 231 However, when the zero wave is allowed to interact with the solution of another neigh-
 232 bouring Riemann problem – such as when multiple Riemann problems are solved on a
 233 sequence of grid cells in a Godunov-type numerical scheme – the local Riemann problems
 234 cannot be taken in isolation.

236 **Zero rarefaction with $C_r > \rho_m$ and $C_l = \rho_m$.**

237 Next we consider the mollified Riemann problem with $C_l = \rho_l = \rho_m$ and $C_r = \rho_r >$
 238 ρ_m . The convex hull and solution are depicted in Fig. 8, and the solution again consists
 239 of a contact line and zero rarefaction wave. The main difference from the previous case
 240 is that the contact line travels to the left with speed $-\gamma$ instead of to the right.

241 Note that since the location of the inflection point of $f_\epsilon(\rho_\epsilon)$ approaches ρ_m as $\epsilon \rightarrow 0$,
 242 an additional zero shock of strength $O(\epsilon^2)$ and speed $O(1/\epsilon)$ is generated. For the sake
 243 of clarity, we have not included this wave in Fig. 8 since it is of higher order than the
 244 $O(\epsilon)$ zero rarefaction and so has negligible impact on the solution in the limit as $\epsilon \rightarrow 0$.

246 4.2. Interaction Between 1-Shock and Zero Rarefaction Wave

247 When solving the double Riemann problem, we need to determine how the zero rar-
 248 efaction wave produced at x_2 interacts with the 1-wave, which we will see shortly must
 249 be a shock. The details of the interaction can be studied using the method of charac-
 250 teristics for the four cases shown in Fig. 6. Since the zero wave has speed $O(1/\epsilon)$, we

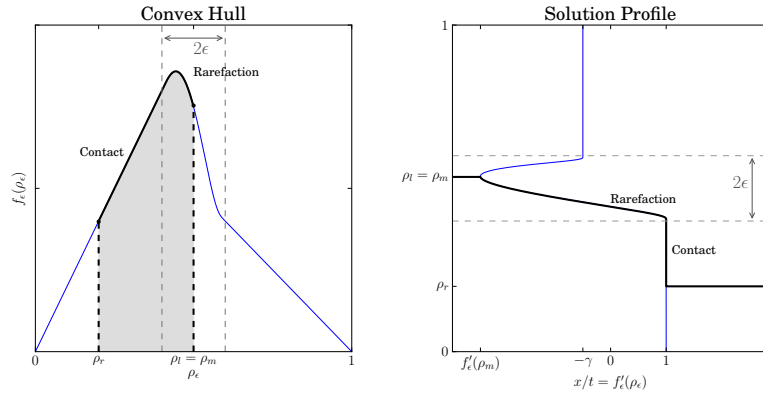


Figure 7: The convex hull (left, shaded) and solution profile (right) for the generation of the zero rarefaction wave when $\rho_l = \rho_m$ and $\rho_r < \rho_m$.

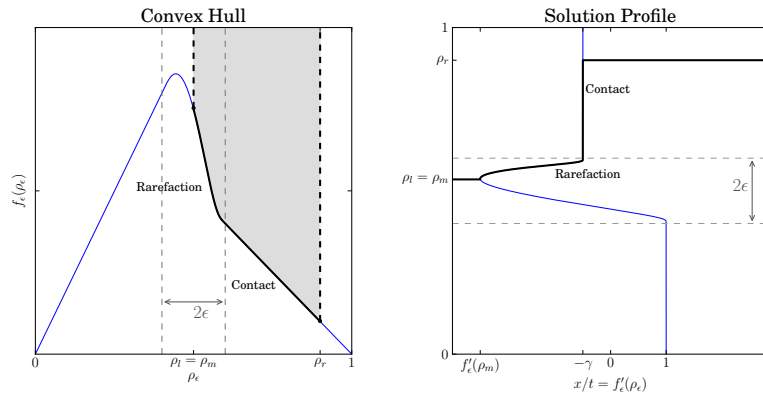


Figure 8: The convex hull (left, shaded) and solution profile (right) for the generation of the zero rarefaction wave when $\rho_l = \rho_m$ and $\rho_r > \rho_m$.

251 must examine the shock-zero rarefaction interaction on two different time scales of length
 252 $O(\epsilon)$ and $O(1)$. Since $\lambda_1 = O(1)$ as $\epsilon \rightarrow 0$ in each case, the problem can be simplified
 253 significantly by neglecting the shock dynamics on the $O(\epsilon)$ time scale. We will then show
 254 that the 1-wave approaches a constant speed as $\epsilon \rightarrow 0$ when $t = O(1)$.

255

256 **Case 1: $C_r, C_l < \rho_m$.**

257 We first consider solutions to the mollified conservation law (6) having initial con-
 258 ditions (20) that satisfy $C_r, C_l < \rho_m$ as shown in Fig. 6(a). The solution in this case
 259 consists of three waves: a shock, a zero rarefaction wave, and a contact line. The initial
 260 discontinuity at x_2 generates a contact line (the 2-wave) that travels at speed $\lambda_2 = 1$,
 261 along with a zero rarefaction wave. A 1-shock originates from location x_1 and travels
 262 along the trajectory $x = S(t)$, where $S(t)$ has yet to be determined. Suppose that the
 263 zero rarefaction wave intersects the 1-wave at time t^* ; then the speed of the 1-wave
 264 satisfies the Rankine-Hugoniot condition

$$\frac{dS(t)}{dt} = \lambda_1(t) = \frac{f_\epsilon(C_l) - f_\epsilon(\rho_m)}{C_l - \rho_m}, \quad \text{for } t \leq t^* \simeq O(\epsilon). \quad (21)$$

265 The time evolution of the solution for $t < t^*$ is illustrated in Fig. 9(b), and the corre-
 266 sponding plot of characteristics in the x, t -plane is shown in Fig. 10. The characteristics
 267 that intersect with the 1-wave for $t < t^*$ have speed equal to 1 to the left of the 1-wave,
 268 and speed $O(1/\epsilon)$ to the right.

269 At time t^* , the zero rarefaction wave starts to interact with the shock $x = S(t)$ which
 270 decreases the density ρ_ϵ to the right of the 1-wave as illustrated in Fig. 9(c). As a result,
 271 the shock wave attenuates leading to an increase in the shock speed λ_1 . Since the zero
 272 wave contains ρ_ϵ values lying within the interval $[\rho_m - \epsilon, \rho_m]$, we can determine the
 273 portion of the shock-zero wave interaction that occurs on the ϵ time scale by finding the
 274 range of ρ_ϵ for which $f'_\epsilon(\rho_\epsilon) = O(1/\epsilon)$. Equation (9) implies that

$$f'_\epsilon(\rho_\epsilon) = O\left(\frac{1}{\epsilon}\eta\left(\frac{\rho_\epsilon - \rho_m}{\epsilon}\right)\right), \quad (22)$$

275 so that we only need to determine the range of ρ_ϵ where

$$\eta\left(\frac{\rho_\epsilon - \rho_m}{\epsilon}\right) = O(1). \quad (23)$$

276 Using the formula for the mollifier (8), it is easy to verify that (23) holds when

$$\rho_\epsilon = \rho_m + \alpha_\epsilon \epsilon, \quad \lim_{\epsilon \rightarrow 0} (\alpha_\epsilon^2 - 1) \neq 0 \quad \text{and} \quad \alpha_\epsilon \in (-1, 1). \quad (24)$$

277 It is only as ρ_ϵ approaches the boundary of the ϵ -region and $\lim_{\epsilon \rightarrow 0} (\alpha_\epsilon^2 - 1) = 0$, that
 278 $f'_\epsilon(\rho_\epsilon) = o(1/\epsilon)$. Therefore, the values of ρ_ϵ within the zero rarefaction wave that satisfy
 279 (24) will interact with the 1-shock on the ϵ time scale.

280 Because $\lambda_1(t) = O(1)$, we can ignore the influence of the shock over the ϵ time scale
 281 when $\epsilon \rightarrow 0$. Therefore, we only need to determine the interaction between the shock
 282 and the zero rarefaction on the $O(1)$ time scale. By finding the range of ρ_ϵ within the
 283 zero wave where $f'_\epsilon(\rho_\epsilon) = O(1)$, we can show that the shock speed λ_1 approaches a

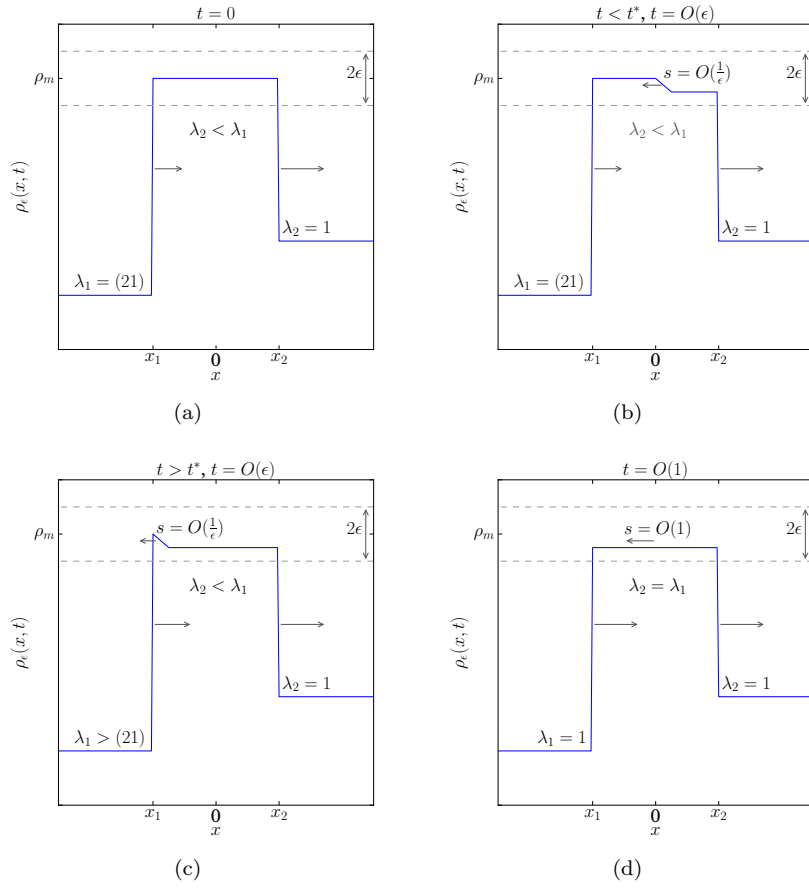
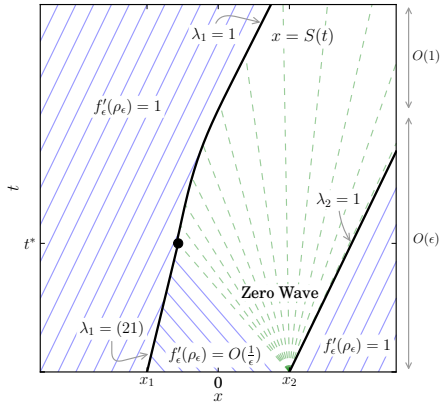
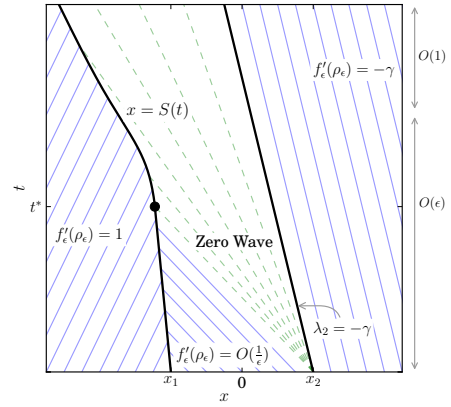


Figure 9: Time evolution of the double Riemann solution in Case 1 when $C_r, C_l < \rho_m$. A similar picture holds in Case 4 when $C_r, C_l > \rho_m$, except that the wave directions are reversed.

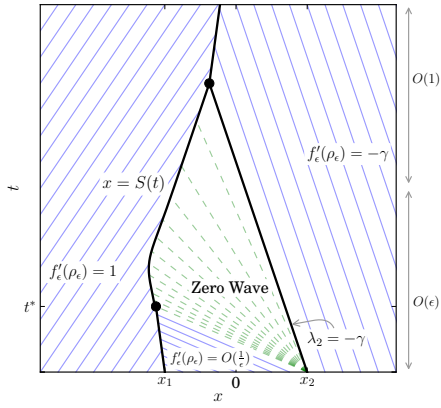
Case 1: $C_r, C_l < \rho_m$



Case 2a: $C_r > \rho_m$ and $\gamma/(\gamma+1) \leq C_l < \rho_m$



Case 2b: $C_r > \rho_m$ and $C_l < \gamma/(\gamma+1) < \rho_m$



Case 3: $C_r < \rho_m < C_l$

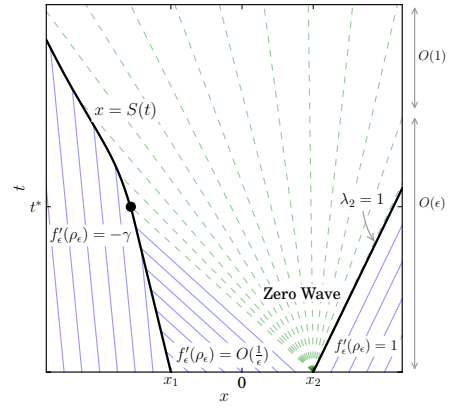


Figure 10: Characteristic lines and elementary waves in the x, t -plane for various cases for the double Riemann solution. The thick lines (black) represent shocks while thin lines (blue and green) represent characteristics.

284 constant as $\epsilon \rightarrow 0$. By using the relationship (22), we know that there exists a ϕ such
 285 that $f'_\epsilon(\rho_\epsilon) = O(1)$ for all

$$\rho_\epsilon = \rho_m - \epsilon + \phi(\epsilon), \quad (25)$$

where $\phi(\epsilon) = o(\epsilon)$ and $\phi(\epsilon) > 0$. Next, by bounding the integral

$$\begin{aligned} \int_{\rho_m - \epsilon}^{\rho_m - \epsilon + \phi(\epsilon)} \eta_\epsilon(s - \rho_m) ds &\leq [\rho_m - \epsilon + \phi(\epsilon) - (\rho_m - \epsilon)] \eta_\epsilon(\rho_m - \epsilon + \phi(\epsilon) - \rho_m), \\ &= \phi(\epsilon) \eta_\epsilon(-\epsilon + \phi(\epsilon)), \\ &= O(\phi(\epsilon)), \end{aligned}$$

we know from Eq. (7) that

$$f_\epsilon(\rho_\epsilon) = \rho_\epsilon + O(\phi(\epsilon)),$$

286 for the range of ρ_ϵ defined by Eqs. (25). Therefore, as $\epsilon \rightarrow 0$, we have that $f_\epsilon(\rho_\epsilon) \rightarrow$
 287 $g_f(\rho_m)$ and the shock speed $\lambda_1 \rightarrow 1$. This results in a solution of the form

$$\rho(x, t) = \begin{cases} C_l, & \text{if } x < x_1 + \lambda_1 t, \\ \rho_m, & \text{if } x_1 + \lambda_1 t \leq x \leq x_2 + \lambda_2 t, \\ C_r, & \text{if } x > x_2 + \lambda_2 t, \end{cases} \quad (26)$$

288 where $\lambda_1 = \lambda_2 = 1$. Therefore, at longer times the solution takes the form of a “square
 289 wave” propagating to the right at constant speed as pictured in Fig. 9(d).

290

291 **Case 2: $C_l < \rho_m < C_r$.**

292 Next, we consider the double Riemann problem when $C_r > \rho_m$ and $C_l < \rho_m$ which
 293 generates a zero rarefaction wave and contact line at x_2 , and a shock at x_1 . Before the
 294 1-shock and zero rarefaction wave interact at time $t^* = O(\epsilon)$, the shock speed λ_1 satisfies
 295 the Rankine-Hugoniot condition (21). For $t > t^*$, the shock and zero rarefaction interact,
 296 thereby causing the value of ρ_ϵ to the right of the 1-wave to increase. Using a similar
 297 argument as in Case 1, we can deduce that when $t = O(1)$,

$$\lambda_1 = \frac{g_c(\rho_m) - f(C_l)}{\rho_m - C_l} \quad \text{and} \quad \lambda_2 = -\gamma, \quad (27)$$

298 as $\epsilon \rightarrow 0$. Note that these wave speeds are consistent with the Riemann problem in
 299 Eq. (17). The time evolution of the solution is illustrated in Fig. 11.

300 There are actually two distinct sub-cases that need to be considered here, correspond-
 301 ing to whether $C_l \geq \gamma/(\gamma + 1)$ (which we call Case 2a) or $C_l < \gamma/(\gamma + 1)$ (Case 2b).
 302 In Case 2a, the two elementary waves (1-shock and 2-contact) do not interact, while in
 303 Case 2b we have $\lambda_1 > \lambda_2$ and so the elementary waves collide to form a single shock that
 304 has speed given by Eq. (19). This distinction is illustrated in the characteristic plots in
 305 Fig. 10.

306

307 **Case 3: $C_r < \rho_m < C_l$.**

308 We next consider the situation when $C_r < \rho_m < C_l$, where a zero rarefaction wave
 309 and contact line are produced at x_2 and a shock wave is generated at x_1 . Before the
 310 1-shock and zero rarefaction wave interact at time $t^* = O(\epsilon)$, the shock speed λ_1 satisfies

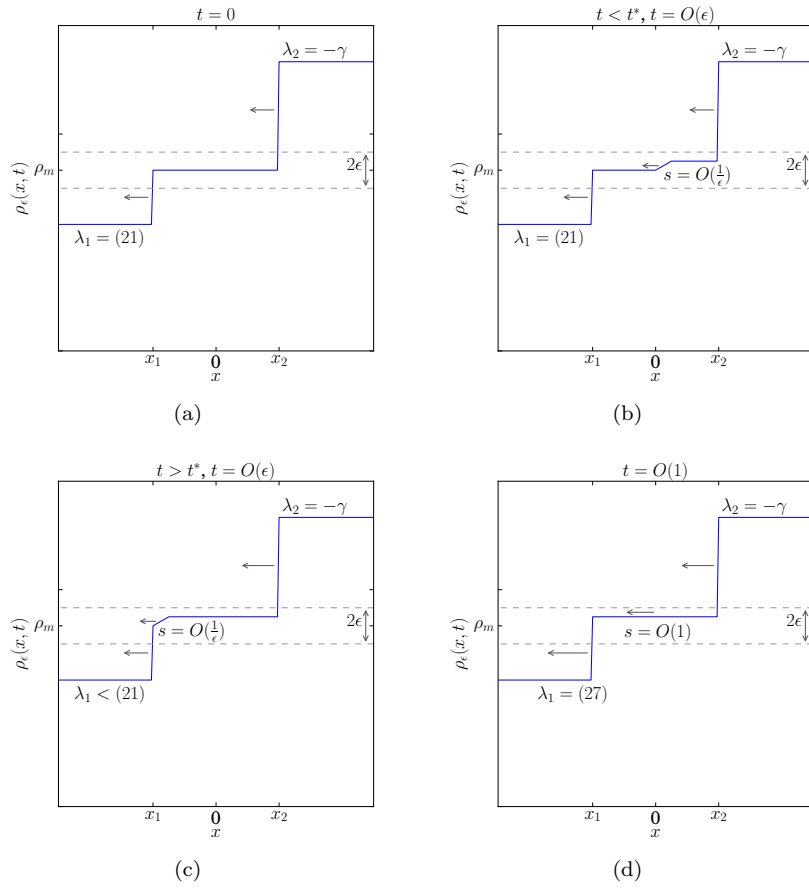


Figure 11: Time evolution of the double Riemann solution in Case 2a when $C_r > \rho_m$ and $\gamma/(\gamma + 1) \leq C_l < \rho_m$.

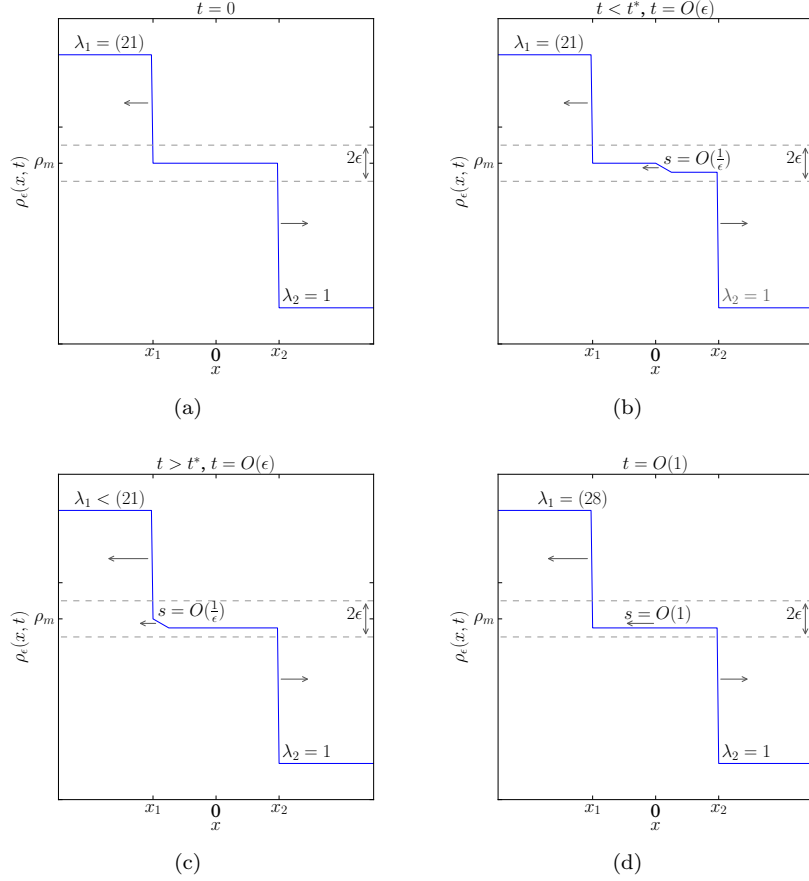


Figure 12: Time evolution of the double Riemann solution in Case 3 when $C_r < \rho_m < C_l$.

311 the Rankine-Hugoniot condition (21) as illustrated in Figs. 12(a) and (b). Once the zero
 312 wave collides with the shock, the shock speed λ_1 increases according to the Rankine-
 313 Hugoniot condition since the value of ρ_ϵ to the right of the 1-wave decreases (shown in
 314 Fig. 12(c)). By ignoring interactions on the $O(\epsilon)$ time scale, we find that

$$\lambda_1 = \frac{g_f(\rho_m) - f(C_l)}{\rho_m - C_l}, \quad \text{and} \quad \lambda_2 = 1, \quad (28)$$

315 for $t = O(1)$ as $\epsilon \rightarrow 0$. Notice that the wave speeds λ_1 and λ_2 are identical to those for
 316 the Riemann problem considered in Case C from Section 3.

317
 318 **Case 4: $C_r, C_l > \rho_m$.**

319 The final remaining case corresponds to $C_r, C_l > \rho_m$ and leads to a solution satisfying

Eq. (26) with

$$\lambda_1 = \frac{g_c(\rho_m) - f(C_l)}{\rho_m - C_l} \quad \text{and} \quad \lambda_2 = -\gamma. \quad (29)$$

The speed of the 1-shock is determined simply by the Rankine-Hugoniot condition where $f(\rho_m)$ is evaluated on the congested flow branch. This should be compared to the 1-wave in Case 3 where the shock speed is determined by Eq. (28) in which $f(\rho_m)$ is evaluated on the free flow branch. No plots of the solution have been provided for Case 4 since the structure is essentially the same as in Case 1 except that all waves propagate in the opposite direction.

5. Finite Volume Scheme of Godunov Type

In this section, we construct a finite volume scheme of Godunov type for our discontinuous flux problem based on ideas originally developed by Godunov [18] for solving the Euler equations of gas dynamics. In Godunov's method, the spatial domain is divided into cells $[x_{j-1/2}, x_{j+1/2}]$ of constant width, $\Delta x = x_{j+1/2} - x_{j-1/2}$, and the solution is assumed to be piecewise constant on each grid cell. Cell-averaged solution values Q_j^n (located at cell centers) are updated using the exact solution from local Riemann problems evaluated at interfaces between adjacent cells. In each time step, the following three-stage algorithm, referred to as the *Reconstruct-Evolve-Average* or *REA algorithm* in [28], is used to update the Q_j^n :

- *Reconstruct* a piecewise constant function $\tilde{\rho}(x, t_n) = Q_j^n$ for all $x \in [x_{j+1/2}, x_{j-1/2}]$ from the cell average Q_j^n at time t_n .
- *Evolve* the conservation law exactly using initial data $\tilde{\rho}(x, t_n)$, thereby obtaining $\tilde{\rho}(x, t_{n+1})$ at time $t_{n+1} = t_n + \Delta t$.
- *Average* the solution $\tilde{\rho}(x, t_{n+1})$ to obtain new cell average values

$$Q_j^{n+1} = \frac{1}{\Delta x} \int_{x_{j-1/2}}^{x_{j+1/2}} \tilde{\rho}(x, t_{n+1}) dx.$$

For problems with smooth flux, the evolution step can be performed by solving a local Riemann problem at each cell interface having left state $\rho_l = Q_j^n$ and right state $\rho_r = Q_{j+1}^n$. As long as the time step is chosen small enough, the elementary waves produced at each interface do not interact (remembering that waves travel at finite speed in the smooth case) and hence the evolution step yields an appropriate approximation of the solution. However, as we have already shown, when the flux is discontinuous the presence of zero waves travelling at infinite speed gives rise to long-range interactions between local Riemann problems. Consequently, we make use of solutions to the double Riemann solution derived in the previous section that incorporate the effects of zero waves. We note that the resulting algorithm has some similarities to the method of Gimse [16].

We next provide details of our implementation using LeVeque's high resolution wave propagation formulation [28], in which the Riemann solver returns a set of wave strengths $\mathcal{W}_{j+1/2}^p$ and speeds $s_{j+1/2}^p$ generated at each interface between states Q_j and Q_{j+1} (in

354 what follows, we will omit the superscript n when it is clear that time index n is assumed).
 355 The *evolution* step of the algorithm above can then be written as

$$Q_j^{n+1} = Q_j^n - \frac{\Delta t}{\Delta x} \left[\sum_p (s_{j-1/2}^p)^+ \mathcal{W}_{j-1/2}^p + \sum_p (s_{j+1/2}^p)^- \mathcal{W}_{j+1/2}^p \right], \quad (30)$$

356 where $(s)^+ = \max(s, 0)$ and $(s)^- = \min(s, 0)$. When the flux is smooth, the wave
 357 speed $s_{j+1/2}$ depends only on the states Q_j and Q_{j+1} , whereas for a discontinuous flux
 358 function this is no longer the case. When $Q_j, Q_{j+1} \neq \rho_m$, the Riemann solver yields the
 359 “standard” elementary waves whose strength and speed are given in Section 3. Because
 360 our flux is strictly non-convex, we also observe compound waves which are described
 361 within Cases 1 and 2 in Section 3.

362 Our Riemann problem solution diverges from the standard one when either $Q_j = \rho_m$
 363 or $Q_{j+1} = \rho_m$, in which case we construct the solution to a local double Riemann
 364 problem that requires the appropriate 1- or 2-wave given in Section 4. Note that the
 365 double Riemann solution should be viewed as two separate local Riemann problems that
 366 each produce one elementary wave: the left Riemann problem corresponds to the 1-wave
 367 and the right Riemann problem corresponds to the 2-wave.

368 For example, if $Q_j = \rho_m$, then we construct the double Riemann problem with
 369 $Q_j = \rho_m$ and $Q_{j+1} = C_r$, thereby obtaining the strength and wave speed corresponding
 370 to the 2-wave in Section 4. Combining together all four cases in Section 4.2, the speed
 371 can be written as

$$s_{j+1/2}^1 = \begin{cases} 1, & Q_{j+1} < \rho_m \\ -\gamma, & Q_{j+1} > \rho_m \end{cases}, \quad (31)$$

372 which we note is independent of C_l .

373 Alternatively, if $Q_{j+1} = \rho_m$ then we construct the double Riemann problem with
 374 $Q_j = C_l$, $Q_{j+1} = \rho_m$ and unknown $Q_I = C_r$, thereby obtaining the strength and wave
 375 speed for the 1-wave in Section 4. In contrast with the case $Q_j = \rho_m$ just considered,
 376 the 1-wave’s speed depends on values of C_l , ρ_m , and C_r . Therefore, when determining
 377 the speed of the wave at the interface between $Q_j = C_l$ and $Q_{j+1} = \rho_m$, we must *look*
 378 *ahead* to find the value $Q_I = C_r$ corresponding to the first value of Q_j not equal to ρ_m ;
 379 that is,

$$I = \min \{ k \mid j+1 < k \leq N \text{ and } Q_k \neq \rho_m \}. \quad (32)$$

380 In summary, when $Q_{j+1}^n = \rho_m$, the wave speed reduces to

$$s_{j+1/2}^1 = \begin{cases} \frac{g_f(\rho_m) - f(Q_j)}{\rho_m - Q_j}, & Q_I < \rho_m \\ \frac{g_c(\rho_m) - f(Q_j)}{\rho_m - Q_j}, & Q_I > \rho_m \end{cases} \quad (33)$$

381 which is visualized in Fig. 13.

382 Note that we have not yet discussed the two simple cases when $Q_j, Q_{j+1} < \rho_m$ and
 383 $Q_j, Q_{j+1} > \rho_m$, both of which reduce to the linear advection equation and can be trivially
 384 solved. A summary of wave strengths and speeds for all cases is presented in Table 1.

385 A slight modification to the local Riemann solver is required to deal with the fact
 386 that algebraic operations are actually performed in floating-point arithmetic. It is highly

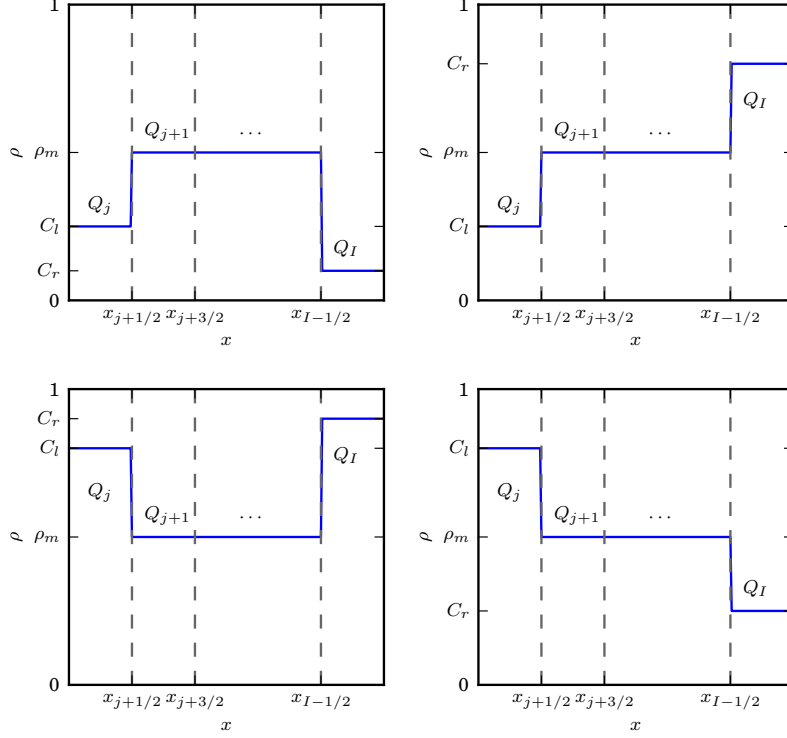


Figure 13: The four possible cases that can arise when calculating the shock speed in Eq. (33).

Table 1: Wave speed and strength for the 1- and 2-waves in all possible cases.

Case	$s_{j+1/2}^1$	$\mathcal{W}_{j+1/2}^1$	$s_{j+1/2}^2$	$\mathcal{W}_{j+1/2}^2$
$Q_j = Q_{j+1} = \rho_m$	0	0	0	0
$Q_j = \rho_m$ and $Q_j \neq Q_{j+1}$	Eq. (31)	$Q_{j+1} - Q_j$	0	0
$Q_{j+1} = \rho_m$ and $Q_j \neq Q_{j+1}$	Eq. (33)	$Q_{j+1} - Q_j$	0	0
$\rho_m < Q_j$ and $\rho_m < Q_{j+1}$	$-\gamma$	$Q_{j+1} - Q_j$	0	0
$\rho_m > Q_j$ and $\rho_m > Q_{j+1}$	1	$Q_{j+1} - Q_j$	0	0
$Q_j < \rho_m < Q_{j+1}$ and $\frac{\gamma}{\gamma+1} \geq Q_j$	$\frac{f(Q_{j+1}) - f(Q_j)}{Q_{j+1} - Q_j}$	$Q_{j+1} - Q_j$	0	0
$\frac{\gamma}{\gamma+1} < Q_j < \rho_m < Q_{j+1}$	$-\gamma$	$Q_{j+1} - \rho_m$	$\frac{g_c(\rho_m) - f(Q_j)}{\rho_m - Q_j}$	$\rho_m - Q_j$
$Q_{j+1} < \rho_m < Q_j$	$\frac{f(Q_j) - g_f(\rho_m)}{Q_j - \rho_m}$	$\rho_m - Q_j$	1	$Q_{j+1} - \rho_m$

387 unlikely that the numerical value of Q_j ever exactly equals ρ_m , and yet we find that it is
 388 necessary to employ the solution of the double Riemann problem when Q_j is *close to* ρ_m .
 389 Therefore, we need to relax the requirement slightly for the zero-wave cases by replacing
 390 the condition $Q_j = \rho_m$ with

$$|Q_j - \rho_m| \leq \delta, \quad (34)$$

391 where δ is a small parameter that is typically assigned values on the order of 10^{-5} . The
 392 choice of δ is a balance between accuracy and efficiency in that taking a larger δ value
 393 gives rise to significant deviations in the height of the ρ_m plateau regions, and hence also
 394 errors in mass conservation. Taking δ values much smaller than 10^{-5} does not improve the
 395 solution significantly but does require a smaller time step for stability. This modification
 396 influences the accuracy of the simulations and also creates an artificial upper bound on
 397 the maximum wave speed, not including zero waves. For example, consider the shock
 398 solution in Eq. (17), where as ρ_l approaches ρ_m the shock speed becomes unbounded.
 399 By enforcing (34), the parameter δ determines how close ρ_l can be to ρ_m before the
 400 algorithm switches to the double Riemann solution.

The time step Δt is chosen adaptively to enforce stability of our explicit update
 scheme, using a restriction based on the wave speeds from all local Riemann problems.
 In particular, we take

$$\Delta t = \text{CFL} \cdot \min_{j,p} \left(\frac{\Delta x}{|s_{j+1/2}^p|} \right),$$

401 where $0 < \text{CFL} < 1$ is a constant chosen to be around 0.9 in practice. As long as the
 402 parameter δ is not taken too small, this condition is sufficient to guarantee stability.
 403 Because the effects of the zero waves have been incorporated directly into the Riemann
 404 problem, they have no direct influence on the stability restriction.

405 The Riemann solver described above forms the basis for the first-order Godunov
 406 scheme. We have also implemented a high resolution variant using *wave limiters* which
 407 limit the waves $\mathcal{W}_{j+1/2}^p$ in a manner similar to the limiting of fluxes in flux-based finite
 408 volume schemes. The details of this modification are described in [28].

409 6. Numerical Results

410 We now apply the method described in the previous section to a number of test
 411 problems. For the high resolution scheme, we employ the superbee limiter function. In
 412 all cases, we use the discontinuous, piecewise linear flux function (3)–(4) with parameters
 413 $\rho_m = 0.5$ and $\gamma = 0.5$ that is pictured in Fig. 14.

414 6.1. Riemann Initial Data

415 As a first illustration of our numerical method, we use three sets of Riemann initial
 416 data:

- 417 A. $\rho_l = 0.9$ and $\rho_r = 0.2$,
- 418 B. $\rho_l = 0.4$ and $\rho_r = 0.9$,
- 419 C. $\rho_l = 0.3$ and $\rho_r = 0.98$,

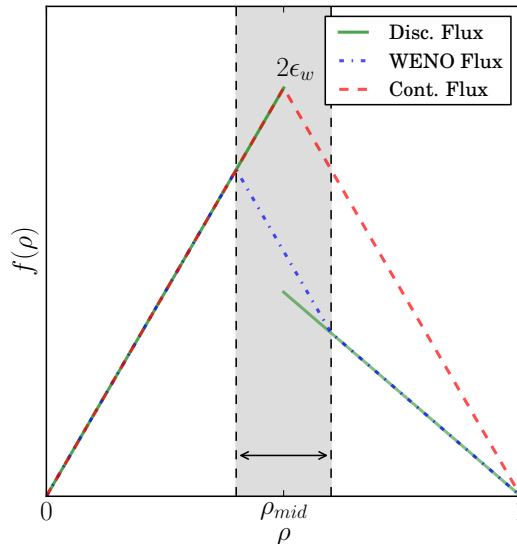


Figure 14: Plots of the discontinuous flux function used in our high resolution simulations (with $\rho_m = 0.5$, $\gamma = 0.5$), the regularized flux for WENO calculations in Section 6.2, and the continuous flux used in Section 6.3.

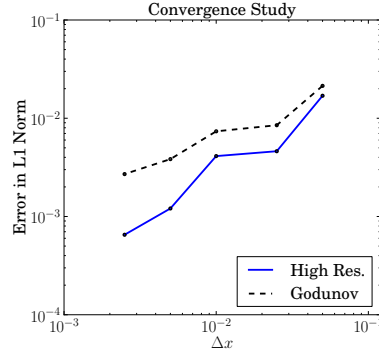
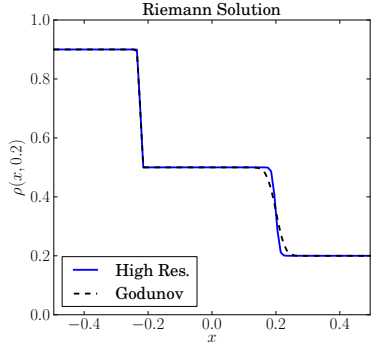
420 for which the exact solution can be determined using the methods in Sections 3 and
 421 4. These initial data labeled A, B and C correspond to the three “Cases” with the
 422 same labels in Section 3 and pictured in Figs. 3, 4 and 5 respectively. We note that the
 423 numerical values for the left and right states in Case C differ slightly from the initial
 424 data used in Fig. 5 in order to generate larger wave speeds.

425 In Fig. 15 (left), we compare the results from the first order Godunov method and
 426 the high resolution scheme with wave limiters. In each case, we perform a convergence
 427 study of error in the discrete L1 norm for grid resolutions ranging from $\Delta x = 0.05$ to
 428 0.0025. Convergence rates estimated using a linear least squares fit are summarized in
 429 Table 2. As expected, the numerical scheme converges to the exact solution for all three
 430 test problems. Godunov’s method captures the correct speed for both the shock and
 431 contact discontinuities, although there is a more noticeable smearing of the contact line
 432 which is typical for this type of problem. The L1 convergence rates are consistent with
 433 the order $\sqrt{\Delta x}$ spatial error estimate established analytically for discontinuous solutions
 434 of hyperbolic conservation laws having a smooth flux [26, 32]. The convergence rates
 435 in the L2 norm are also provided for comparison purposes and are significantly smaller
 436 than the corresponding L1 rates, as expected.

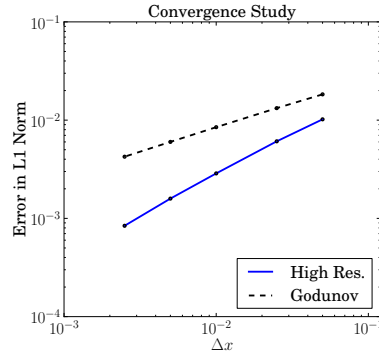
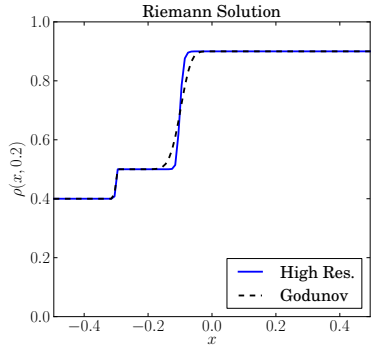
437 6.2. Smooth Initial Data, With WENO Comparison

438 For the next series of simulations, we use the smooth initial data

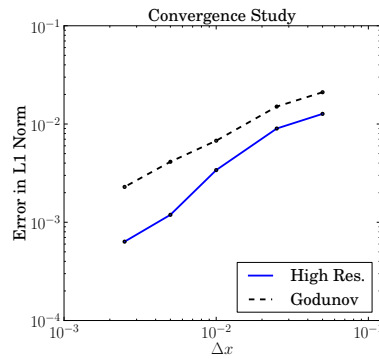
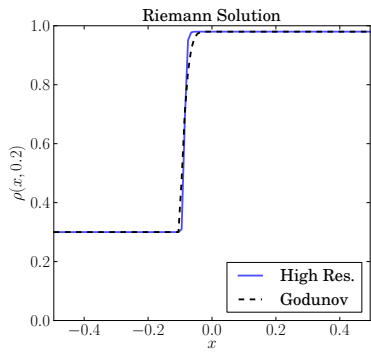
$$\rho(x, 0) = \exp\left(-\frac{x^2}{2\sigma^2}\right), \quad (35)$$



(a)



(b)



(c)

Figure 15: Left: Computed solutions for the Riemann initial data at $t = 0.2$ where $\delta = 10^{-7}$, $\Delta x = 0.01$, CFL = 0.95, $\rho_m = 0.5$, and $\gamma = 0.5$. Right: Convergence study in the L1 norm.

Table 2: Convergence rates for the three Riemann problems pictured in Fig. 15.

		Godunov		High Resolution	
ρ_l	ρ_r	L1	L2	L1	L2
0.9	0.2	0.643	0.367	1.022	0.569
0.4	0.9	0.488	0.232	0.832	0.375
0.3	0.98	0.754	0.373	1.053	0.627
0.1	0.4	0.487	0.145	0.700	0.238

439 where $\sigma = 0.1$ and the domain is the interval $[-1, 1]$ with periodic boundary conditions.
440 This corresponds in the traffic flow context to a single platoon of cars travelling on a ring
441 road, where the initial density peak has a maximum value of 1 and decreases smoothly
442 to zero on either side. Fig. 16 depicts the time evolution of the solution computed using
443 our high resolution Godunov scheme. Initially, the platoon begins to spread out and a
444 horizontal plateau appears on the right side at a value of $\rho = \rho_m$. This plateau value
445 corresponds to the “optimal” traffic density that is the maximum value of ρ for which cars
446 can still propagate at the free-flow speed. The plateau lengthens as a shock propagates
447 to the left into the upper half of the density profile, reducing the width of the peak.
448 At the same time, the cars in the dense region spread out to the right as the plateau
449 also extends in the same direction, while the left edge of the platoon remains essentially
450 stationary until the dense peak is entirely gone. When the peak finally disappears (near
451 time $t = 0.18$), the remaining platoon of cars propagates to the right with constant speed
452 and unchanged shape. Note that the traffic density evolves such that the area under the
453 solution curve remains approximately constant, since the total number of cars must be
454 conserved.

455 For comparison purposes, we have also performed simulations using the WENO
456 scheme in CentPack [2], which employs a third-order CWENO reconstruction in space
457 [25, 29] and a third-order SSP Runge-Kutta time integrator [19]. Because this algo-
458 rithm requires the flux function to be continuous (although not smooth), we have used
459 a regularized version of the flux that is piecewise linear and continuous, replacing the
460 discontinuity by a steep line segment connecting the two linear pieces over a narrow
461 interval of width $2\epsilon_w$ (instead of using the function f_ϵ in (7) because that would require
462 an integral to be evaluated for every flux function evaluation). The regularized flux is
463 shown in Fig. 14.

464 From Fig. 16, we observe that the WENO simulation requires a substantially smaller
465 time step and grid spacing in order to obtain results that are comparable to our method.
466 In particular, the WENO scheme requires a time step of $\Delta t = O(10^{-6})$ and a spatial
467 resolution of $\Delta x = O(10^{-4})$ when $\epsilon_w = 10^{-3}$; this can be compared with our high
468 resolution Godunov scheme for which we used a time step of $\Delta t = O(10^{-4})$ when $\Delta x =$
469 $O(10^{-3})$ and $\delta = 10^{-5}$. This performance difference is magnified further as ϵ_w decreases
470 due to the ill-conditioning of the regularized-flux problem.

471 In Fig. 17, we magnify the region containing the density peak at time $t = 0.1$ to more

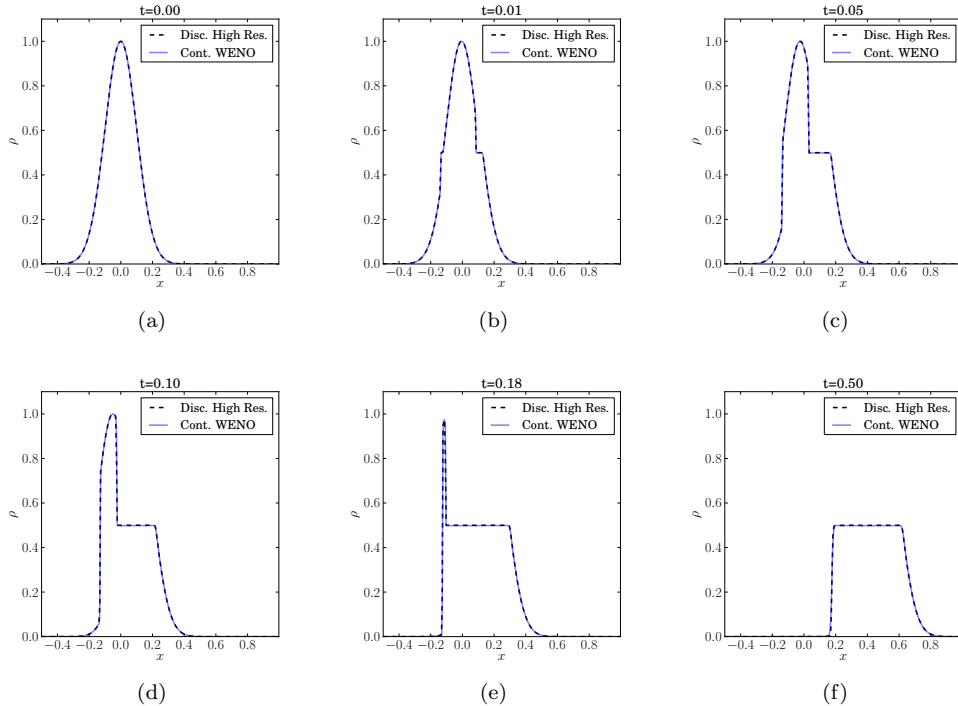


Figure 16: Time evolution of the solution with smooth initial conditions using a high resolution scheme ($\delta = 10^{-5}$, $\Delta x = 0.005$, CFL = 0.9) and a third-order WENO scheme [2] ($\Delta x = 0.0004$, $\epsilon_w = 10^{-3}$, CFL = 0.9) where $\rho_m = 0.5$ and $\gamma = 0.5$.

472 easily visualize the difference between the two sets of results for different values of ϵ_w
 473 and δ . From these plots we observe that the two solutions approach one another as both
 474 ϵ_w and δ are reduced, which provides further evidence that our high resolution Godunov
 475 scheme computes the correct solution. Note that the WENO scheme does yield a slightly
 476 sharper resolution of the shock than our method, but on the other hand it significantly
 477 underestimates the height of the plateau region when ϵ_w is too large.

478 Next, we estimate the error in our high resolution Godunov scheme by comparing
 479 the computed solutions on a sequence of successively finer grids with $\Delta x_p = \Delta x_0/3^p$ for
 480 $p = 0, 1, \dots, P$, with $P = 6$ levels of refinement. The finest grid solution with $\Delta x = \Delta x_P$
 481 is treated as the “exact” solution for the purposes of this convergence study. The errors
 482 at $t = 0.05$ shown in Fig. 18(a) exhibit convergence rates of approximately 1.125 in the L1
 483 norm and 0.632 in the L2 norm which are consistent with the results from Section 6.1. We
 484 note that even though the initial data are smooth, our high resolution Godunov scheme
 485 does not obtain second order accuracy because of the shock that appears immediately
 486 on the right side of the plateau.

Because convergence rates provide only a rough measure of solution error, we can
 gain additional insight into the accuracy of the method by measuring *conservation error*,

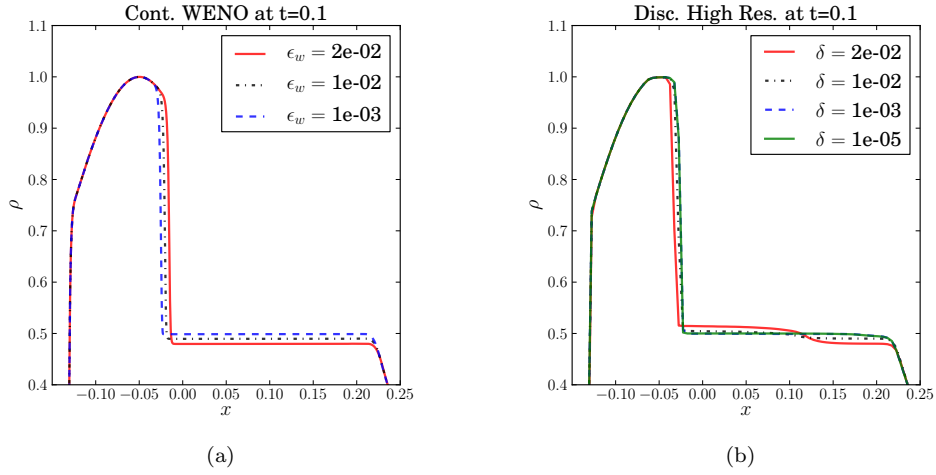


Figure 17: (a) WENO simulation for different ϵ_w for problem pictured in Fig. 16 where $\Delta x = 0.0004$ and $\Delta t = O(10^{-6})$. (b) High resolution simulation for different δ for problem pictured in Fig. 16 where $\Delta x = 0.005$ and $\Delta t = O(10^{-4})$.

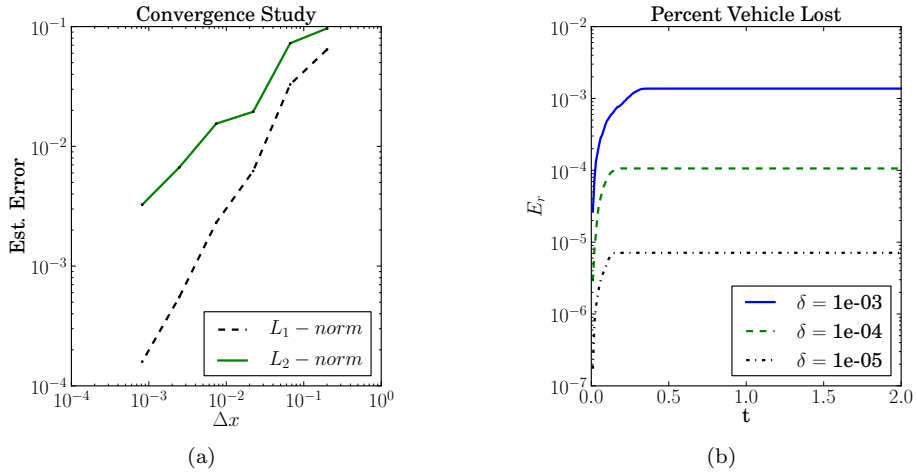


Figure 18: (a) Convergence study for the problem with smooth initial data at $t = 0.05$ using $\Delta x_0 = 0.2$ and $P = 6$ levels of refinement (refer to Fig. 16). (b) Percentage of the initial vehicles lost during the simulation using different δ values.

which is expressed in terms of the variation V in the total number of vehicles via

$$E_r = \frac{V^n - V^0}{V^0} \quad \text{where} \quad V^n = \Delta x \sum_{j=1}^N Q_j^n.$$

487 Since we are using periodic boundary conditions and have no external sources or sinks,
 488 V^n should remain approximately constant for all n . Indeed, Fig. 18(b) shows that the
 489 numerical scheme accumulates only a small conservation error over time, and that the
 490 rate of vehicles lost can be controlled by reducing δ .

491 6.3. Smooth Initial Data, With Continuous Flux Comparison

492 In this final set of simulations, we compare solutions of the conservation law (3) with
 493 the discontinuous piecewise linear flux (4) and the continuous piecewise linear flux

$$f_c(\rho) = \begin{cases} \rho, & \text{if } 0 \leq \rho < \rho_m, \\ \frac{\rho_m}{1 - \rho_m}(1 - \rho), & \text{if } \rho_m \leq \rho \leq 1. \end{cases} \quad (36)$$

494 Both fluxes are illustrated in Fig. 14.

495 We begin by emphasizing that these two seemingly very different flux functions can
 496 still give rise to similar solutions to the Riemann problem with suitably chosen piece-
 497 wise constant initial data. For Cases A and C from Section 3, the convex hulls and
 498 the corresponding solutions are identical for the two fluxes. However, the convex hulls
 499 are different in Case B, where the discontinuous flux gives rise to the compound wave
 500 illustrated in Fig. 4 while the continuous flux generates a single shock (analogous to the
 501 solution in Fig. 5). Furthermore, the continuous flux (36) does not give rise to any zero
 502 waves; instead, when either $\rho_l = \rho_m$ or $\rho_r = \rho_m$, a single contact line is produced that
 503 satisfies the Rankine-Hugoniot condition.

504 A clear illustration of the difference between these two fluxes is provided by comparing
 505 simulations on the periodic domain $x \in [-1, 1]$ for smooth initial data

$$\rho(x, 0) = \frac{1}{2} \exp\left(-\frac{x^2}{2\sigma^2}\right) + \frac{2}{5}, \quad (37)$$

506 where $\sigma = 0.1$. This corresponds to the situation where there is a Gaussian-shaped
 507 congestion in the middle of free-flow traffic on a ring road.

508 Fig. 19 depicts the time evolution of the solution computed using a high resolution
 509 Godunov scheme for the continuous and discontinuous fluxes. Note that the numeri-
 510 cal solution for the discontinuous flux requires application of the look-ahead procedure
 511 discussed in Section 5 while the continuous flux requires only the calculation of interac-
 512 tions between adjacent cells. Initially, the congested region begins to spread out and a
 513 horizontal plateau appears on the right side at a value of $\rho = \rho_m$. On the left edge of
 514 this plateau, a shock appears for the discontinuous flux in comparison with a gradual
 515 continuous variation in density for the continuous flux.

516 The solutions are more drastically different when comparing the dynamics on the left
 517 edge of the congested region. For the discontinuous flux, a compound wave forms to the
 518 left of the peak, resulting in the formation of a second horizontal plateau at the maximum
 519 congested flow speed $\rho = \rho_m$. Therefore, drivers on the far left will enter into a optimal

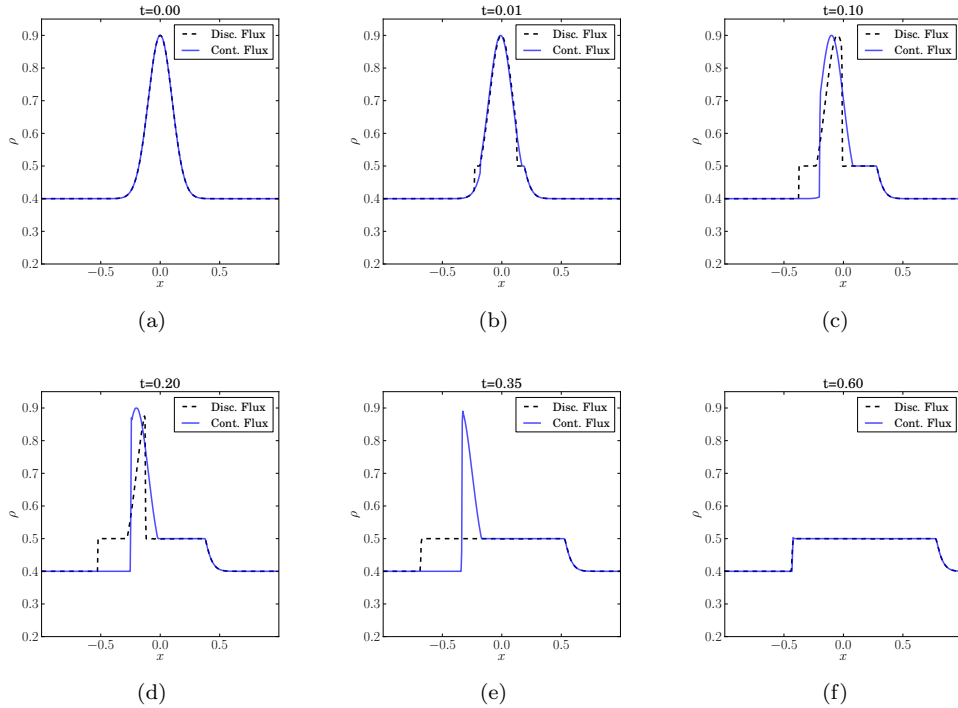


Figure 19: Time evolution of the solution with smooth initial conditions using a high resolution scheme ($\delta = 10^{-5}$, $\Delta x = 0.005$, CFL = 0.9) for both the smooth and discontinuous flux.

520 congested flow before being hit by the left-moving congestion wave. The continuous flux,
 521 on the other hand, produces only a single left-moving congestion wave.

522 We conclude therefore that if the fundamental diagram is discontinuous, we expect to
 523 observe compound congestion waves. The leading congestion wave acts to push vehicles
 524 into some form of optimal congested flow, possibly a synchronized traffic state. This wave
 525 is followed up by a slower congestion wave. Note that we only expect these compound
 526 congestion waves when the upstream free flow traffic has sufficiently high density. For
 527 example, in Fig. 16, we observed only a single congestion shock because the traffic density
 528 to the left is too small to sustain this compound congestion wave.

529 7. Conclusions

530 In this paper, we derived analytical solutions to the Riemann problem for a hyperbolic
 531 conservation law with a piecewise linear flux function having a discontinuity at the point
 532 $\rho = \rho_m$. In the case when the left and right states in the Riemann initial data lie on
 533 either side of the discontinuity, the solution consists of a compound wave made up of a
 534 shock and contact line connected by a constant intermediate state at ρ_m . In the special
 535 case when either the left or right state equals ρ_m , the Riemann problem gives rise to a

536 zero rarefaction wave that propagates with infinite speed. Even though the strength of
537 this wave is zero, it nonetheless has a significant impact on the solution structure as it
538 interacts with other elementary waves.

539 Our analytical results were validated using a high resolution Godunov-type scheme,
540 based on our exact Riemann solver and implemented using the wave propagation for-
541 malism of LeVeque [28]. This approach builds the effect of zero waves directly into the
542 algorithm in a way that avoids the overly stringent CFL time step constraint that might
543 otherwise derive from the infinite speed of propagation of zero waves. We demonstrate
544 the accuracy and efficiency of our method using several test problems, and include com-
545 parisons with higher-order WENO simulations.

546 We conclude with a brief discussion of several possible avenues for future research.
547 First, a detailed convergence analysis of the algorithm would help to identify non-smooth
548 error components that arise from the discontinuity in the flux, as well as the look-ahead
549 procedure required to determine shock speeds in the case when $\rho_m = \rho_l$ or ρ_r . Sec-
550 ond, we would like to consider other nonlinear forms of the piecewise discontinuous flux
551 function since the linearity assumption in this paper simplifies our analytical solutions
552 considerably in that elementary waves arising from local Riemann problems consist of
553 shocks and contact lines only. For example, it would be interesting to perform a detailed
554 comparison with the results of Lu et al. [31] who considered a discontinuous, piecewise
555 quadratic flux. Thirdly, we mention some preliminary computations of traffic flow using
556 a cellular automaton model [37] that give rise to an apparent discontinuity in the funda-
557 mental diagram. This connection between cellular automaton models (that only specify
558 rules governing individual driver behaviour) and kinematic wave models (in which the
559 two-capacity effect is incorporated explicitly via the flux function) merits further study.
560 Finally, the situation where the flux is a discontinuous function of the spatial variable
561 has been analyzed much more extensively (see the journal issue introduced by the article
562 [6], and references therein). We would like to draw deeper connections between this work
563 and the problem where the discontinuity appears in the density.

564 References

- 565 [1] D. Armbruster, S. Göttlich, and M. Herty. A scalar conservation law with discontinuous flux for
566 supply chains with finite buffers. *SIAM J. Appl. Math.*, 71(4):1070–1087, 2011.
- 567 [2] J. Balbas and E. Tadmor. CentPack. Available on-line at [http://www.cscamm.umd.edu/centpack/](http://www.cscamm.umd.edu/centpack/software)
568 `software`, July 2006.
- 569 [3] J. H. Bank. Two-capacity phenomenon at freeway bottlenecks: a basis for ramp metering. *Transp.*
570 *Res. Rec.*, 1320:83–90, 1991.
- 571 [4] J. H. Bank. The two-capacity phenomenon: some theoretical issues. *Transp. Res. Rec.*, 1320:234–
572 241, 1991.
- 573 [5] R. Bürger, A. García, K. H. Karlsen, and J. D. Towers. Difference schemes, entropy solutions,
574 and speedup impulse for an inhomogeneous kinematic traffic flow model. *Netw. Heterog. Media*,
575 3(1):1–41, 2008.
- 576 [6] R. Bürger and K. H. Karlsen. Conservation laws with discontinuous flux: A short introduction. *J.*
577 *Engrg. Math.*, 60(3):241–247, 2008.
- 578 [7] A. Ceder. A deterministic traffic flow model for the two-regime approach. *Transp. Res. Rec.*,
579 567:16–30, 1976.
- 580 [8] R. M. Colombo. Hyperbolic phase transitions in traffic flow. *SIAM J. Appl. Math.*, 63(2):708–721,
581 2002.
- 582 [9] C. F. Daganzo. Requiem for second-order fluid approximations of traffic flow. *Transp. Res. B*,
583 29(4):277–286, 1995.

- 584 [10] J. P. Dias and M. Figueira. On the Riemann problem for some discontinuous systems of conservation
585 laws describing phase transitions. *Commun. Pure Appl. Anal.*, 3:53–58, 2004.
- 586 [11] J. P. Dias and M. Figueira. On the approximation of the solutions of the Riemann problem for a
587 discontinuous conservation law. *Bull. Braz. Math. Soc.*, 36(1):115–125, 2005.
- 588 [12] J. P. Dias and M. Figueira. On the viscous Cauchy problem and the existence of shock profiles for
589 a p-system with a discontinuous stress function. *Quart. Appl. Math.*, 63(2):335–341, 2005.
- 590 [13] J. P. Dias, M. Figueira, and J. F. Rodrigues. Solutions to a scalar discontinuous conservation law
591 in a limit case of phase transitions. *J. Math. Fluid Mech.*, 7(2):153–163, 2005.
- 592 [14] S. M. Easa. Selecting two-regime traffic-flow models. *Transp. Res. Rec.*, 869:25–36, 1982.
- 593 [15] L. C. Edie. Car-following and steady-state theory for noncongested traffic. *Opns. Res.*, 9(1):66–76,
594 1961.
- 595 [16] T. Gimse. Conservation laws with discontinuous flux functions. *SIAM J. Math. Anal.*, 24(2):279–
596 289, 1993.
- 597 [17] P. Goatin. The Aw-Rascle vehicular traffic flow model with phase transitions. *Math Comput.
598 Model.*, 44(34):287–303, 2006.
- 599 [18] S. K. Godunov. A difference method for numerical calculation of discontinuous solutions of the
600 equations of hydrodynamics. *Mat. Sb.*, 47:271–306, 1959.
- 601 [19] S. Gottlieb, C. W. Shu, and E. Tadmor. Strong stability-preserving high-order time discretization
602 methods. *SIAM Rev.*, 43(1):89–112, 2001.
- 603 [20] B. D. Greenshields. A study of traffic capacity. *Proc. Highw. Res.*, 14(1):448–477, 1935.
- 604 [21] F. L. Hall, B. L. Allen, and M. A. Gunter. Empirical analysis of freeway flow-density relationships.
605 *Transp. Res. A*, 20(3):197–210, 1986.
- 606 [22] D. Helbing. Traffic and related self-driven many-particle systems. *Rev. Mod. Phys.*, 73:1067–1141,
607 2001.
- 608 [23] B. S. Kerner. *The Physics of Traffic: Empirical Freeway Pattern Features, Engineering Applica-
609 tions and Theory*. Springer, 2004.
- 610 [24] M. Koshi, M. Iwasaki, and I. Ohkura. Some findings and an overview on vehicular flow characteris-
611 tics. In V. F. Hurdle, E. Hauer, and G. N. Steuart, editors, *Proceedings of the Eighth International
612 Symposium on Transportation and Traffic Theory*, pages 403–426, Toronto, Canada, June 24–26,
613 1981. University of Toronto Press.
- 614 [25] A. Kurganov and D. Levy. A third-order semi-discrete central scheme for conservation laws and
615 convection-diffusion equations. *SIAM J. Sci. Comput.*, 22(4):1461–1488, 2000.
- 616 [26] N. N. Kuznetsov. Accuracy of some approximate methods for computing the weak solutions of a
617 first-order quasi-linear equation. *USSR Comput. Math. Math. Phys.*, 16(6):105–119, 1976.
- 618 [27] R. J. LeVeque. Some traffic flow models illustrating interesting hyperbolic behavior. In *Min-
619 isymposium on traffic flow, SIAM Annual Meeting*, July 10, 2001. Available on-line at [http:
620 //faculty.washington.edu/rjl/pubs/traffic/traffic.pdf](http://faculty.washington.edu/rjl/pubs/traffic/traffic.pdf).
- 621 [28] R. J. LeVeque. *Finite Volume Methods for Hyperbolic Problems*. Cambridge University Press, New
622 York, 2002.
- 623 [29] D. Levy, G. Puppo, and G. Russo. Central WENO schemes for hyperbolic systems of conservation
624 laws. *Math. Model. Numer. Anal.*, 33:547–571, 2001.
- 625 [30] M. J. Lighthill and G. B. Whitham. On kinematic waves. II. A theory of traffic flow on long crowded
626 roads. *Proc. Roy. Soc. Lond. A*, 229(1178):317–345, 1955.
- 627 [31] Y. Lu, S. C. Wong, M. Zhang, and C.-W. Shu. The entropy solutions for the Lighthill-Whitham-
628 Richards traffic flow model with a discontinuous flow-density relationship. *Transp. Sci.*, 43(4):511–
629 530, 2009.
- 630 [32] B. J. Lucier. Error bounds for the methods of Glimm, Godunov and LeVeque. *SIAM J. Numer.
631 Anal.*, 22(6):1074–1081, 1985.
- 632 [33] S. Martin and J. Vovelle. Convergence of implicit finite volume methods for scalar conservation
633 laws with discontinuous flux function. *Math. Model. Numer. Anal.*, 42(5):699–727, 2008.
- 634 [34] O. Oleinik. Uniqueness and stability of the generalized solution of the Cauchy problem for a
635 quasilinear equation. *Amer. Math. Soc. Transl.*, 2(33):285–290, 1964.
- 636 [35] B. N. Persaud and F. L. Hall. Catastrophe theory and patterns in 30-second freeway traffic data –
637 Implications for incident detection. *Transp. Res. A*, 23A(2):103–113, 1989.
- 638 [36] P. I. Richards. Shock waves on a highway. *Opns. Res.*, 4:42–51, 1956.
- 639 [37] J. K. Wiens. Kinematic wave and cellular automaton models for traffic flow. Master’s thesis,
640 Department of Mathematics, Simon Fraser University, Burnaby, Canada, Aug. 2011. Available
641 on-line at <http://theses.lib.sfu.ca/thesis/etd6760>.
- 642 [38] G. C. K. Wong and S. C. Wong. A multi-class traffic flow model - an extension of LWR model with

- 643 heterogeneous drivers. *Transp. Res. A*, 36(9):827–841, 2002.
- 644 [39] N. Wu. A new approach for modeling of fundamental diagrams. *Transp. Res. A*, 36:867–884, 2002.
- 645 [40] H. M. Zhang. Anisotropic property revisited – does it hold in multi-lane traffic? *Transp. Res. B*,
- 646 37(6):561–577, 2003.
- 647 [41] H. M. Zhang and T. Kim. A car-following theory for multiphase vehicular traffic flow. *Transp. Res.*
- 648 *B*, 39(5):385–399, 2005.